Batteries & Supercaps

Research Article
doi.org/10.1002/batt.202500015

Chemistry Europe
European Chemical Societies Publishing

www.batteries-supercaps.org

Sodium Manganese Hexacyanoferrate: Characterization as Sodium-Ion Battery Cathode Material, Full Cell Cycling with Hard Carbon and Post-Mortem Analyses

Sebastian Büchele,*[a, b] Valeriu Mereacre,[a] Nicole Bohn,[a] Pirmin Stüble,[a] Xuebin Wu,[a] Noah Keim,[a] Ruochen Xu,[a] Holger Geßwein,[a] Wenzhe Sun,[a] Grigor Vrhovac,[a] Michael Pordzik,[a] Thomas Bergfeldt,[a] Sylvio Indris,[a, c] Werner Bauer,[a] Helmut Ehrenberg,[a] and Joachim R. Binder[a]

Sodium manganese hexacyanoferrate $Na_2Mn[Fe(CN)_6]$ (NaMn*HCF*) is a promising cathode material for sodium-ion batteries, owing to its voltage profile similar to that of lithium iron phosphate (LFP) and its use of abundant, inexpensive resources. This study presents full cell cycling data for NaMn*HCF* against hard carbon (HC) anodes with various common carbonate-based electrolytes across different voltage windows. Post-mortem analyses indicate that, in addition to NaMn*HCF* degradation, Na^+-ion inventory loss significantly contributes to capacity decline during cycling. Surprisingly, an ICP-OES analysis of the post-mortem anodes show that the correct electrolyte choice can entirely prevent the commonly cited manganese dissolution of NaMn*HCF* during cycling. This work also highlights methods for characterizing and processing NaMn*HCF* and the broader Prussian White family of materials, helping to introduce these materials to a wider audience. Finally, a comparison between NaMn*HCF*/HC and LFP/graphite is provided, examining both cost and electrochemical performance.

1. Introduction

Lithium-ion batteries (LIBs) play an important role in the world's transition to sustainable energy. However, due to the rapidly growing demand for energy storage in electric cars and stationary storage, lithium is expected to run into supply gaps.[1] Sodium-ion batteries (SIBs) might play a crucial role in the energy storage market as they can bring some relief to the lithium supply chains. They are considered a drop-in technology, which means that they can be manufactured in existing LIB production facilities with only minor adjustments. By choosing the active materials wisely, SIBs can contain only abundant and therefore cheap elements whose resources are distributed worldwide.

The best-known material for the SIB anode is hard carbon (HC), which for instance can be obtained from bio-based materials.[2–4] For the SIB cathode there are three main classes of material. As with LIBs, there are *(i)* layered oxides and *(ii)* polyanionic materials. In addition, *(iii)* the Prussian Blue analogs – which are not well explored in the LIB space – have attracted a lot of attention as SIB cathode material.[5]

Polyanionic materials such as $Na_4Fe_3(PO_4)_2P_2O_7$, $Na_3V_2(PO_4)_3$, and $Na_3V_2(PO_4)_2F_3$ demonstrate excellent cycling stability but suffer from low conductivity and challenges such as limited specific energy or reliance on costly elements like vanadium.[6–9] Similarly, layered oxides offer high energy density but face issues including sodium deficiency, structural instability, air sensitivity, or the use of expensive resources like nickel and copper.[10–12] Moreover, the production processes for both material classes are similar to their lithium-ion counterparts, such as lithium iron phosphate (LFP or $LiFePO_4$) and lithium layered oxides (e.g., $LiNi_{0.8}Mn_{0.1}Co_{0.1}O_2$ or NMC811), negating the potential for reduced processing costs. This further complicates their ability to compete with the overall production costs of LFP, as discussed later.

The Prussian Blue analogs date back to the historically relevant color pigment "Berlin Blue", which was developed by Johann Jacob Diesbach in Berlin in 1706 and soon became known as "Prussian Blue" due to the bright blue color of Prussian military uniforms. The early crystal framework of these materials contained only iron, carbon and nitrogen. In addition to its use as a pigment, it is also used as an oral medication named "Radiogardase" developed by the Berlin company Heyl for victims of poisoning with radioactive caesium or thallium, as was the case during the nuclear accident in Fukushima.[13,14]

Beginning in 2012 the works of John B. Goodenough's group drew a wider attention to the Prussian Blue class as a battery material, as it can reversibly store alkali metal ions, especially lithium, sodium and potassium.[15–17] In the context of

---

[a] *S. Büchele, V. Mereacre, N. Bohn, P. Stüble, X. Wu, N. Keim, R. Xu, H. Geßwein, W. Sun, G. Vrhovac, M. Pordzik, T. Bergfeldt, S. Indris, W. Bauer, H. Ehrenberg, J. R. Binder*
Institute for Applied Materials, Karlsruhe Institute of Technology, 76344 Eggenstein-Leopoldshafen, Germany
E-mail: sebastian.buechele@kit.edu

[b] *S. Büchele*
Litona GmbH, Helmholtzstraße 8/2, 89081 Ulm, Germany

[c] *S. Indris*
Applied Chemistry and Engineering Research Centre of Excellence (ACER CoE), Université Mohammed VI Polytechnique (UM6P), Lot 660, Hay Moulay Rachid, Ben Guerir, 43150, Morocco

batteries, it is common to refer to a Prussian Blue analog as Prussian Blue when it is only partially filled with alkali metal ions. When the structure is completely filled with alkali metal ions, it is called Prussian White; when it is empty, it is called Prussian Yellow.[13] Some cell designs, such as that of Natron Energy in the USA, use two sodium Prussian Blue analogs with different transition metals and therefore different potentials vs. Na^+/Na, the key being that both sides are initially only partially filled with sodium-ions, because if both were fully filled, the sodium-ions would not be able to shuttle between both electrodes.[18]

In a SIB with a HC anode, however, the cathode should initially be fully filled. Among these sodium Prussian Whites, sodium iron hexacyanoferrate (NaFe*HCF*, ideally $Na_2Fe[Fe(CN)_6]$), currently commercialized by Altris in Sweden, and sodium manganese hexacyanoferrate (NaMn*HCF*, ideally $Na_2Mn[Fe(CN)_6]$) are the best known.[19] NaMn*HCF* is particularly interesting due to its higher potential plateau vs. Na^+/Na at 3.47 V compared to that of NaFe*HCF* at 3.0 and 3.3 V.[19]

If SIBs are to coexist sustainably with LIBs on the mass market in the future and not just fill lithium supply gaps, they must have a real advantage over LIBs. Apart from soft advantages such as, their better low-temperature performance, the possibility to use aluminum as current collector for both electrodes and their ability to withstand deep discharge without damage, unlike LIBs, the biggest advantage is the potential cost reduction.[20] However, it is easy to overlook how good the low cost LIB chemistry is, which uses LFP and graphite and is very popular for electric vehicles and stationary storage.[21]

The costs of a battery cell can be divided into material costs and production costs, with the material costs accounting for the largest share. The aforementioned drop-in capability of SIBs in LIB production processes also means that the production cost of SIBs are unlikely to be cheaper than that of LIBs.[22] Furthermore, HC might not be cheaper than graphite, especially not natural graphite. This means that the entire cost advantage of SIBs due to the cathode material.[23]

Therefore, a material cost comparison of LFP with NaMn*HCF* is of relevant interest. Since the LFP material cost mainly depends on the lithium carbonate price, Figure 1 shows the fluctuations of this cost over the last five years. Lithium carbonate was cheapest in 2020 at 8.6 $\$ kg^{-1}$ and most expensive in 2022 at 68.1 $\$ kg^{-1}$.

Table 1 shows the material cost comparison of LFP and NaMn*HCF* based on their raw material cost in 2023 and the aforementioned cost range for lithium carbonate from 2019 to 2023. Note that a direct comparison in $\$ kg^{-1}$ of LFP and NaMn*HCF* is valid since both materials have roughly the same specific energy of ~500 Wh kg^{-1}, as shown in section 3.2 of this study. Furthermore, a conservative additional cost for the synthesis of NaMn*HCF* is assumed, which Xu *et al.* attributed to the cost of sodium citrate.[25]

The LFP material cost totals between 5.48 and 19.39 $\$ kg^{-1}$ depending on the lithium carbonate price, while the cost of NaMn*HCF* is <4.56 $\$ kg^{-1}$. This means that when lithium carbonate prices are high, NaMn*HCF* is substantially less costly than LFP. However, when the lithium carbonate price is low, the material cost of LFP is only slightly higher than that of NaMn*HCF*. Since the synthesis of NaMn*HCF* does not require calcination, unlike LFP, the cost of production of NaMn*HCF* could potentially reduce the overall cost of the material relative to LFP. This is an important advantage to exploit in NaMn*HCF* to ensure that it, and therefore the SIBs that are built with it, can remain cheaper than an LFP LIB in all circumstances. This would increase the rate of success of SIBs finding their place on the mass market alongside LIBs in the long term.

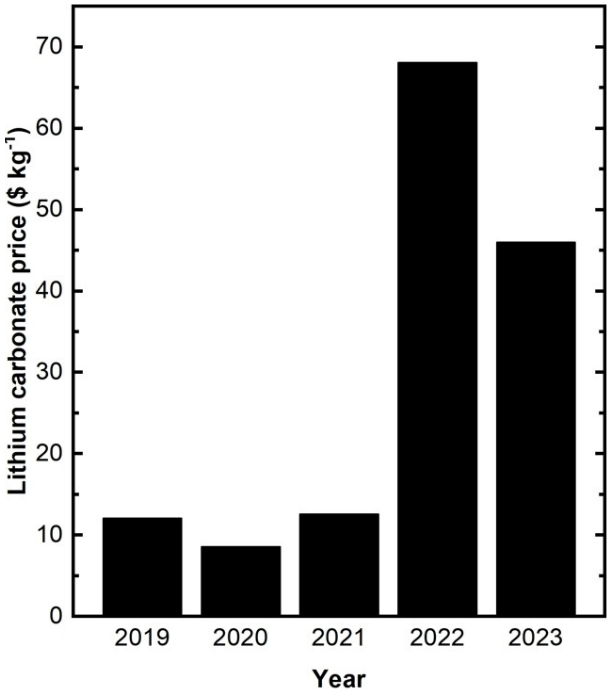

Figure 1. Annual average-nominal price for battery-grade lithium carbonate (Li_2CO_3).[24]

Table 1. Material costs for LFP and NaMn*HCF* based on raw material costs in 2023. A price range as shown in Figure 1 was used for lithium carbonate. Adapted and modified from Xu *et al.*[25]

Raw materials	Price ($\$ kg^{-1}$)	LFP ($\$ kg^{-1}$)	NaMn*HCF* ($\$ kg^{-1}$)
Li_2CO_3	8.60 – 68.00	2.02 – 15.92	
$FePO_4$	3.60	3.47	
$MnSO_4$	1.08		0.59
$Na_4Fe(CN)_6$	1.26		1.97
Addition	<2.00		<2.00
Sum		**5.48 – 19.39**	$<$**4.56**

Beyond economic factors, NaMn*HCF* faces significant technological challenges, especially in achieving the cycling stability required to rival LFP. This study aims to provide a better understanding of the current status of NaMn*HCF* and its performance compared to LFP. For this purpose, NaMn*HCF* cathodes, formulated with an active material content of 88% to be close to industry standards, were assembled in coin full cells with HC anodes and tested with different electrolytes. After cycling, cells were disassembled for post-mortem analyses, including half cell cycling of the post-mortem cathodes to isolate NaMn*HCF* degradation and to study its contribution to full cell capacity loss. Further investigation involved detecting Na, Mn, and Fe on the anodes to evaluate transition metal dissolution and in-situ X-ray diffraction (XRD).

Given the novelty of Prussian White materials in battery applications, this study also covers specific characterization and handling protocols for NaMn*HCF*, emphasizing the critical role of a tailored drying step prior to cell assembly – a requirement distinct to this material class. This methodological discussion highlights essential practices needed to optimize NaMn*HCF* for high-performance sodium-ion batteries.

2. Results

2.1. NaMn*HCF* Characterization

This section provides a basis for the characterization and understanding of Prussian White materials in battery cell applications, with a focus on NaMn*HCF*. Here, the chemical composition of the investigated NaMn*HCF* powder is determined and a detailed analysis of the vacancy content, theoretical capacity and water content is performed. In addition, the drying process required to benefit from full electrochemical performance is carried out.

2.1.1. Powder Properties

Figure 2a shows a photograph of the investigated NaMn*HCF*, which appears white in its fully sodiated form. Figure 2b shows a scanning electron microscopy (SEM) image of the NaMn*HCF*, which shows cubic particles of several μm in size. A particle size distribution (PSD) measurement gives an average particle size of 5.8 μm with a distribution of $D_{10}=3.4$ μm, $D_{50}=5.6$ μm and $D_{90}=8.7$ μm. The specific surface area was measured to be at 1.6 $m^2 g^{-1}$ using the Brunauer-Emmet-Teller (BET) method.

2.1.2. Chemical Composition by Inductively Coupled Plasma Optical Emission Spectroscopy (ICP-OES)

The ideal chemical composition of NaMn*HCF* as a cathode material is $Na_2Mn^{II}[Fe^{II}(CN)_6]$. It has a molar mass of 312.9 g mol^{-1} and a theoretical specific capacity of 171.3 mAh g^{-1}, as two Na^+-ions can reversibly intercalate into the structure per formula unit. During charging, Mn and Fe atoms are oxidized from oxidation state +II to +III so that the Na^+-ions can deintercalate from the crystal structure. During discharge, their oxidation state is reduced from +III to +II in order to re-insert Na^+-ions into the structure. This also means that after synthesis, all Mn and Fe atoms should be in oxidation state +II so that the material is fully sodiated.

However, in reality the chemical composition of NaMn*HCF* after synthesis is $Na_xMn_{1-y}^{(II/III)}[Fe^{(II/III)}(CN)_6]_{1-z} \bullet w\ H_2O$ with a Na-content $x<2$, Mn vacancies $y<1$, $[Fe(CN)_6]^{3-/4-}$ vacancies $z<1$ and crystal/vacancy water $w \geq 0$.[19,26,27] For the sake of simplicity, it is assumed that the very stable $[Fe(CN)_6]^{4-}$ complexes are all intact. Furthermore, it can be assumed that Mn vacancies in the NaMn*HCF* structure occur very rarely or not at all. This is due to the fact that the NaMn*HCF* channel radius is 1.6 Å and Mn-ions have an ionic radius <1 Å and can therefore fill possible Mn vacancies after the crystal has already been formed if the synthesis duration is sufficiently long. $Fe(CN)_6$-ions have an ionic radius of 3.57 Å and cannot easily diffuse in the crystal to fill occurring vacancies afterwards.[13] $[Fe(CN)_6]^{4-}$ vacancies are therefore much more likely than Mn vacancies.

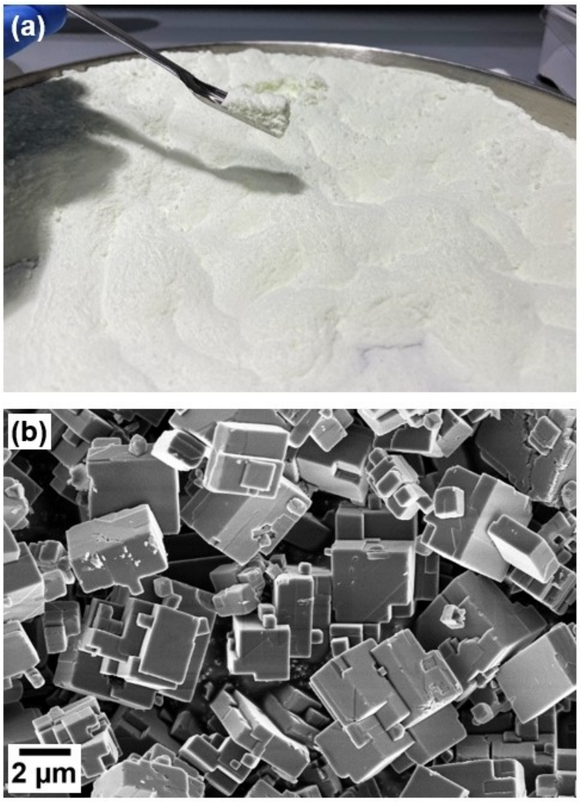

Figure 2. (a) Photograph and (b) SEM image of NaMn*HCF* powder.

To determine the chemical composition of the investigated NaMn*HCF*, the molar ratios of Na, Mn and Fe were analyzed by ICP-OES. Under the hypothesis that the investigated NaMn*HCF* has no Mn vacancies, the calculated chemical composition normalized to the Mn content is $Na_{1.80}Mn[Fe(CN)_6]_{0.95} \cdot w\ H_2O$.[19,26,27]

2.1.3. Validation of Calculated Chemical Composition

To validate the calculated chemical composition of $Na_{1.80}Mn[Fe(CN)_6]_{0.95}$, it is possible to verify the claimed 5% $[Fe(CN)_6]^{4-}$ vacancies. For every missing $[Fe(CN)_6]^{4-}$ complex, four missing negative charges must be compensated for. This is done by reducing four neighboring Mn atoms to an oxidation state +II.

Usually, a Mn atom that is incorporated into the NaMn*HCF* structure with an oxidation state of +II pulls in a Na^+-ion to balance the charge. However, these four Mn atoms in oxidation state +II compensate for the missing negative charges and do not attract an additional Na^+-ion into the structure. Therefore, one $[Fe(CN)_6]^{4-}$ vacancy leads to four missing Na^+-ions in the NaMn*HCF* structure.[19] Thus, 5% $[Fe(CN)_6]^{4-}$ vacancies lead to a theoretical Na content in the NaMn*HCF* structure of $x = 2 - 4 \cdot 0.05 = 1.80$. This is exactly the Na content we calculated from the ICP-OES results, thus confirming our hypothesis that there are no Mn vacancies in the investigated NaMn*HCF*. Furthermore, this means that the investigated NaMn*HCF* is completely sodiated after synthesis, i.e. all Mn and Fe atoms are reduced to an oxidation state of +II. Otherwise the Na content of the NaMn*HCF* would have to be lower than 1.80 per sum formula.

The question whether all the Fe atoms in the NaMn*HCF* structure are in the +II oxidation state can be answered by Fe Mössbauer spectroscopy. Figure 3 shows the Mössbauer spectrum of the NaMn*HCF* powder and shows only a single contrinution with isomer shift of (-0.08 ± 0.01) mm/s. This peak can be assigned to Fe^{2+} in low-spin state and the presence of Fe^{3+} can be excluded.[28] This indicates that all Fe atoms in the NaMn*HCF* structure are in the +II oxidation state, which further confirms the calculated chemical composition.

2.1.4. Theorectical Specific Capacity

Figure 4 shows the theoretical specific capacity of NaMn*HCF* as a function of the amount of $[Fe(CN)_6]^{4-}$ vacancies *z*, assuming that no Mn vacancies are present, all Mn and Fe atoms are reduced to an oxidation state of +II and all Na^+-ions can reversibly be removed of the structure. The sum formula $Na_{2-4z}Mn^{(II)}[Fe^{(II)}(CN)_6]_{1-z}$ was used to calculate the figure. It can be seen that the specific capacity decreases quadratically with increasing $[Fe(CN)_6]^{4-}$ vacancy content. It starts at 171.3 mAh g^{-1} for 0% $[Fe(CN)_6]^{4-}$ vacancies and drops to 0 mAh g^{-1} for 50% $[Fe(CN)_6]^{4-}$ vacancies.

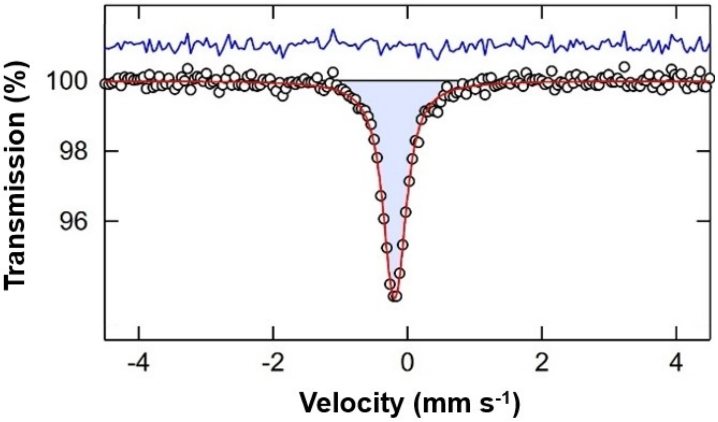

Figure 3. ^{57}Fe Mössbauer spectrum of NaMn*HCF* powder. The experimental data points are shown as white circles, the overall fit as the red line, and the difference as the blue line.

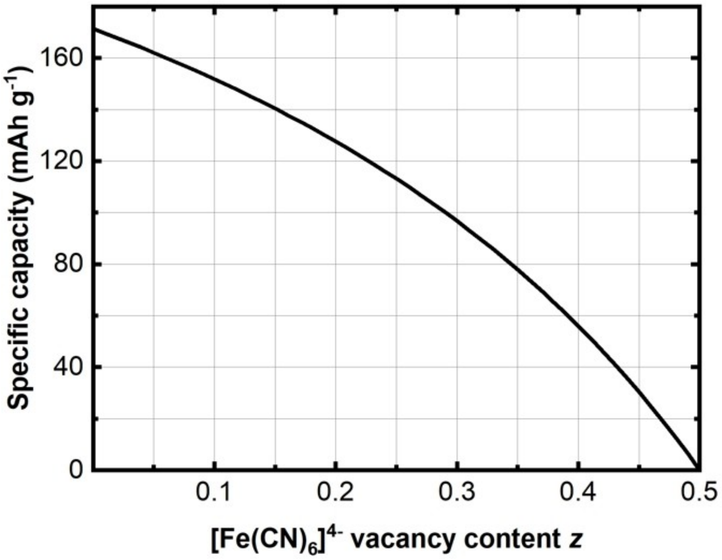

Figure 4. Specific capacity of NaMn*HCF* as a function of the $[Fe(CN)_6]^{4-}$ vacancy content *z*, assuming that no Mn vacancies are present and all Mn and Fe atoms are reduced to oxidation state +II. The resulting theoretical sum formula is $Na_{2-4z}Mn^{(II)}[Fe^{(II)}(CN)_6]_{1-z}$.

The previously identified sum formula of $Na_{1.80}Mn[Fe(CN)_6]_{0.95}$ corresponds to a molar mass of 297.7 g mol^{-1} and a theoretical specific capacity of 162.1 mAh g^{-1}.

2.1.5. Water Content and Drying

As shown in previous work on Prussian White, the drying step has proven to be crucial for good electrochemical performance.[16,29] Thereby it is important to differentiate between the drying of surface water and crystal water.

Surface water can be easily removed from NaMn*HCF*, for example, by simply storing the material at ambient temperature for 24 h under inert conditions.[30] This is usually done after synthesis, before the NaMn*HCF* is stored in a dry room or in an inert gas atmosphere. This is necessary because NaMn*HCF* degrades in a two-step process when exposed to both water and oxygen over an extended period of time, as shown by Ojwang *et al.*[31] However, short-term exposure to ambient air and thus water and oxygen does not severely degrade the material. For this reason, NaMn*HCF* can be mixed in an aqueous slurry and coated without the need for special treatment of the water, as shown by Hartmann et al. and applied in this work.[32]

Crystal water, on the other hand, does not cause NaMn*HCF* to degrade over time. However, Goodenough *et al.* found that removing crystal water changes the crystal structure of NaMn*HCF* from monoclinic to rhombohedral. The rhombohedral crystal structure occurs in NaMn*HCF* when it is fully sodiated and free of crystal water, while the monoclinic structure occurs when NaMn*HCF* is fully sodiated but still contains crystal water.[16] Since the rhombohedral structure offers superior electrochemical performance, it is essential to remove the crystal water before cell assembly through proper drying. Unlike surface water, the crystal water cannot be removed simply by a drying step at ambient pressure. In fact, recent research by Maddar *et al.* has shown that a high-quality vacuum (~10^{-3} mbar) is crucial for the removal of crystal water.[33]

Figure 5 shows the XRD patterns of pristine powder and electrodes that were prepared with pristine NaMn*HCF* powder and were only dried in the electrode. The XRD pattern of the pristine powder is shown as a reference in Figure 5a. The prepared electrodes were dried for 15 h either at 120 °C and 1.5 mbar (see Figure 5b) or 80 °C and $3 \cdot 10^{-3}$ mbar (see Fig 5c). While the pristine NaMn*HCF* powder shows reflections originating from the monoclinic crystal structure with space group symmetry $P2_1/n$, the electrode dried at 120 °C and 1.5 mbar in addition shows a small reflection at 18° from the rhombohedral structure (see Figure 5b). The electrode in Figure 5c, which was only dried at 80 °C but at a better vacuum of $3 \cdot 10^{-3}$ mbar, shows mainly reflections which can be indexed to the rhombohedral crystal structure with space group symmetry R-3. Additionally a minor peak at 34° 2θ can be attributed to the presence of a small amount of a cubic Fm-3 m phase which was formed during the drying process.

This shows that a temperature of 80 °C is sufficient to remove the crystal water from the investigated NaMn*HCF* if the

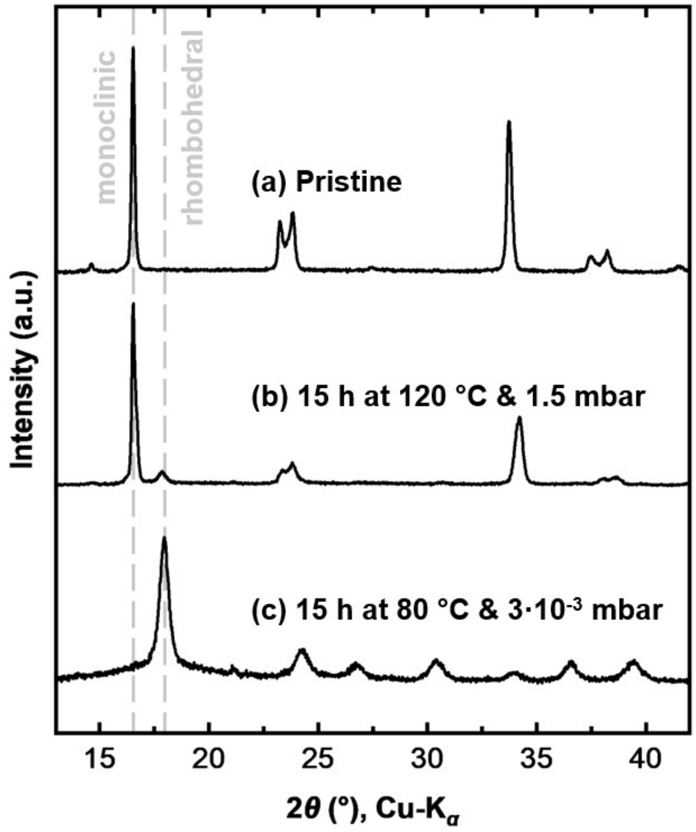

Figure 5. XRD patterns of NaMn*HCF* electrodes that were (a) not dried or dried for 15 h at (b) 120 °C and 1.5 mbar or (c) 80 °C and $3 \cdot 10^{-3}$ mbar.

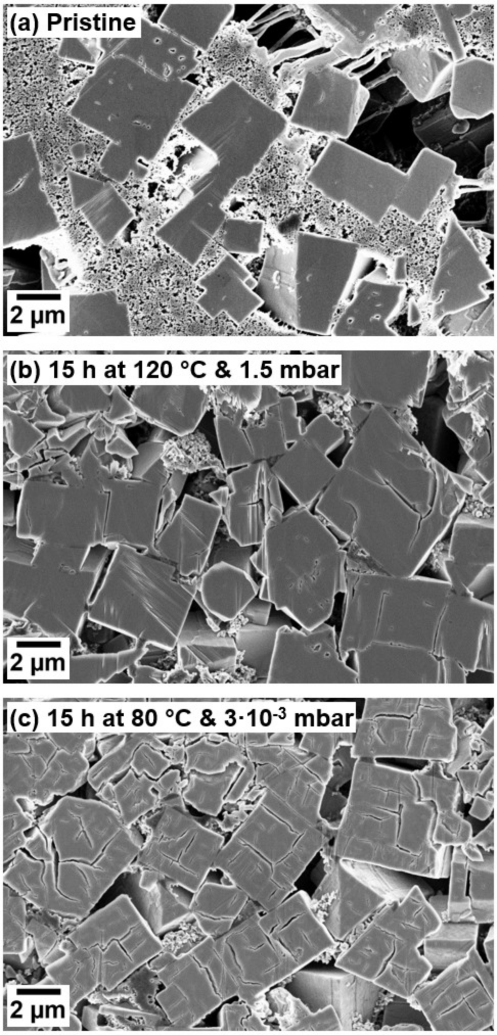

Figure 6. SEM cross-sectional images of NaMn*HCF* (a) pristine powder and electrodes that were dried for 15 h at (b) 120 °C and 1.5 mbar or (c) 80 °C and $3\cdot10^{-3}$ mbar. The pristine powder was embedded in an electrode to create the cross-section.

vacuum level is good enough. In contrast, even a higher temperature of 120 °C is not effective in removing the crystal water if the vacuum is poor, as shown by the 1.5 mbar condition in Figure 5b. It is noticeable that the transition from the monoclinic to the rhombohedral crystal structure is coupled with a broadening of the XRD spectrum. As shown in Figure 6, there is a fragmentation of the monoclinic particles during the drying process; both size and strain effects are likely to occur in the rhombohedral phase and which could explain this observation.

The findings suggest that, in an industrial setting, it may be feasible to dry the electrodes directly without pre-drying the NaMn*HCF* powder. However, the greater thickness of industrial electrodes could pose challenges to achieving effective drying under such conditions.

Figure 6 shows the corresponding SEM cross-sectional images of the NaMn*HCF* powder and electrodes from Figure 5, which were pristine or dried for 15 h at either 120 °C and 1.5 mbar or 80 °C and $3\cdot10^{-3}$ mbar. The particles of the pristine powder in Figure 6a show no cracks, the particles in the poorly dried electrode in Figure 6b show some cracks and the particles of the crystal water free, well-dried NaMn*HCF* electrode in Figure 6c show many cracks. This is consistent with previously reported crack formation that occurs during the crystal structure shift from monoclinic to rhombohedral.[33]

To estimate how much crystal water w the investigated $Na_{1.80}Mn[Fe(CN)_6]_{0.95} \bullet w\ H_2O$ contains after synthesis, a thermogravimetric analysis (TGA) was performed. For this purpose, the powder was even dried at 150 °C instead of only 80 °C at $3\cdot10^{-3}$ mbar to ensure that absolutely no crystal water reamains.

Figure 7 shows TGA data of pristine NaMn*HCF* powder (dashed line) and NaMn*HCF* powder dried at 150 °C and $3\cdot10^{-3}$ mbar for 15 h (solid line). Both powders were previously stored in an Ar atmosphere prior to the TGA test to reduce the amount of surface water present. The pristine powder shows a

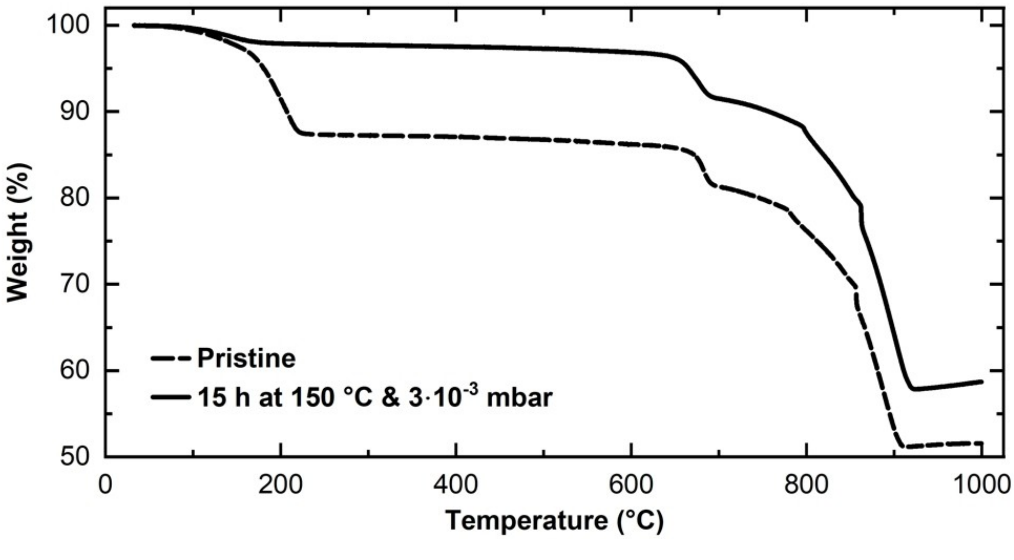

Figure 7. TGA data of NaMn*HCF* powder that was either pristine (dashed line) or previously dried for 15 h at 150 °C and $3\cdot10^{-3}$ mbar (solid line). The powders were heated from 25 to 1,000 °C at 5 K min^{-1} in an Ar atmosphere.

severe weight loss of 12.6% up to 220 °C, while the dried powder only shows a weight loss of 2.0% in this temperature range. This indicates that the NaMn*HCF* powder mainly loses water in the first 220 °C. The 2.0% weight loss observed in the dried NaMn*HCF* powder is most likely due to water adsorption during the brief exposure of the powder to ambient air during the preparation of the TGA sample. This weight loss is observed below 150 °C, which means that this water would already be eliminated in the dried sample during the drying step at 150 °C (see solid line, Figure 7).

The weight loss at temperatures above 220 °C is similar for both samples. The powder masses remain approximately constant until 630 °C before decreasing in several distinct steps up to 920 °C. The mass decreases by an approximately total of 41% above 220 °C in both cases, relative to the mass at 220 °C, which indicates the same decomposition mechanism.

Assuming that the initial weight loss of 12.6% of the pristine powder is entirely due to the loss of crystal water, the chemical composition of the investigated NaMn*HCF* powder in this work is $Na_{1.80}Mn[Fe(CN)_6]_{0.95}$ 2.38 H_2O

2.2. NaMn*HCF* Full Cell Cycling with HC

This section presents NaMn*HCF* cycling data of half cells with a sodium metal anode and full cells with a HC anode using different electrolytes. For this purpose, the NaMn*HCF* electrodes were dried for 15 hours at 130 °C and $3\cdot10^{-3}$ mbar, exceeding the minimum required 80 °C to ensure that no crystal water remained in the structure, while staying below a temperatures that could damage the electrodes' binders. The cycling was carried out at C/5 in order to allow sufficient time for any time-dependent parasitic reactions as to not exclude calendar ageing. In addition, the voltage window of commercial LFP/graphite cells (2.5 to 3.65 V) is used for the NaMn*HCF*/HC cells to observe how much capacity is lost compared to the full voltage window and how the cycling performance is affected.

2.2.1. Cycling in Wide Voltage Window (1.5 – 4.0 V)

Figure 8 shows the C/5 cycling data of NaMn*HCF*/HC full cells prepared with different electrolytes, cycled from 1.5 to 4.0 V. After every 50 cycles two C/20 check-up cycles were done. The electrolytes used were based on Dreyer *et al.* and were 1 м $NaPF_6$ in a 3:7 volume ratio of ethylene carbonate and diethyl carbonate (EC:DEC, red circles), 1 м $NaPF_6$ in a 1:1:1 volume ratio of EC, propylene carbonate (PC) and dimethyl carbonate (DMC) + 5 vol% fluoroethylene carbonate (FEC, purple triangles) and 1 м $NaClO_4$ in a 1:1:1 volume ratio of EC:PC:DMC + 5 vol% FEC (green stars).[34] Additionally, a NaMn*HCF* half cell cycled from 2.0 V to 4.1 V with 1 м $NaPF_6$ in PC + 5 wt% FEC as the electrolyte is shown (black squares). All experiments were conducted using paired cells, with each cell tested with an identical counterpart under the same conditions. The paired cells consistently showed similar behavior, but were not plotted for clarity.

The half cell starts with a C/20 discharge capacity of 154.1 mAh g^{-1}, which drops to 143.0 mAh g^{-1} at C/5. The NaMn*HCF*/HC full cells start with a lower initial discharge capacity of approximately 139 mAh g^{-1} at C/20, which is due to irreversible capacity loss associated to the solid electrolyte interphase (SEI) formation on HC during the first charge and the consequent Na$^+$-ion inventory loss. The capacity drops to around 132 mAh g^{-1} at C/5. The different electrolytes in the full cells cause no difference in initial discharge capacity or in C-rate

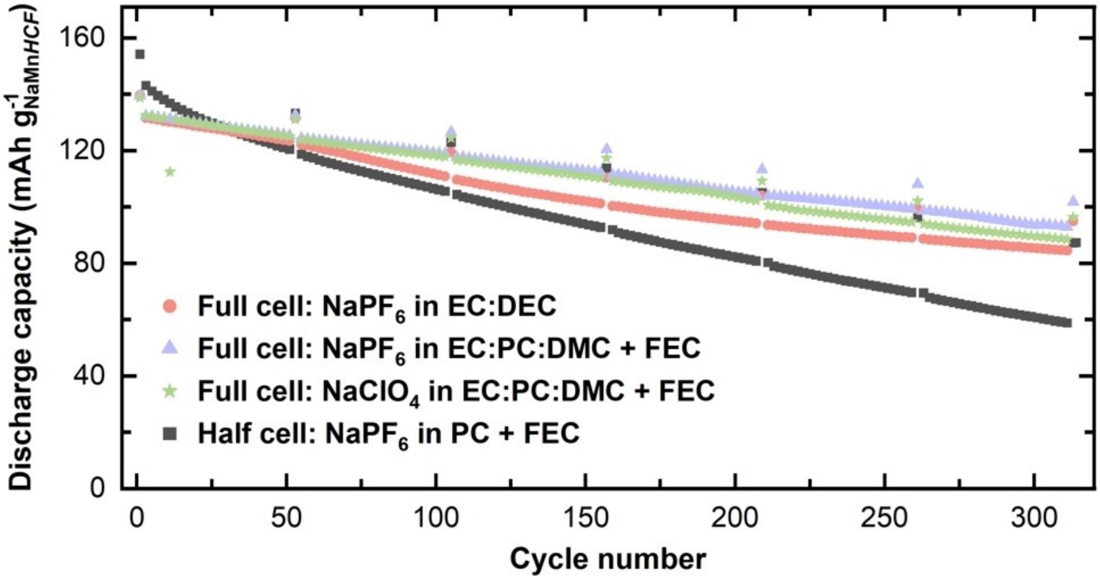

Figure 8. Cycling data of full cells with NaMn*HCF* cathode and HC anode cycled from 1.5 to 4.0 V at 23 °C with different electrolytes. In addition, a coin half cell with a NaMn*HCF* cathode and sodium metal anode cycled from 2.0 V to 4.1 V (black squares) is shown. After two initial C/20 cycles with a constant-voltage (CV) step to C/50 at the upper cut-off voltage, cycling continued at C/5 with a CV step to C/20. After every 50 cycles two C/20 check-up cycles were done. For a better visualization, only every second cycle is displayed.

capability. However, electrolyte choice influences the capacity retention of the full cells. The $NaPF_6$ in EC:PC:DMC + FEC electrolyte shows the best cycling stability and retains 72.9 % of its original C/20 capacity after 314 cycles (purple). Replacing $NaPF_6$ with $NaClO_4$ results in a very similar capacity retention up to 200 cycles before the $NaClO_4$ electrolyte shows greater degradation (green). $NaPF_6$ in EC:DEC performed the worst of all the full cell electrolytes tested, retaining only 67.9 % of its original C/20 capacity after 314 cycles (red). Interestingly, the NaMn*HCF* half cell shows a much worse cycling stability, retaining only 56.6 % of its original capacity after 314 cycles (based on the C/20 check-up cycles). A possible explanation is that NaMn*HCF* undergoes complete Na^+ intercalation and deintercalation during each cycle in the half cell. In contrast, the irreversible Na loss during the initial cycle in full cells results in only partial reintercalation of Na^+ in subsequent cycles. As a result, NaMn*HCF* operates at a reduced capacity, experiencing less stress, which enhances capacity retention. Baumgart *et al.* simulated a complete transition from the cubic to the rhombohedral phase, estimating a volume reduction of up to 20 % for the unit cell.[35] However, this volume change is less pronounced in real-life scenarios where residual crystal water is present, as demonstrated by Guo *et al.*[36] Their study highlighted that crystal water acts as structural pillars, reducing volume changes during electrochemical cycling.

It is worth noting that the difference between the C/20 and C/5 capacity is much larger for the half cell compared to the full cells and even increases with consecutive cycling. Whereas the C/5 and C/20 full cell capacities differ only by 5 – 10 $mAh\,g^{-1}$ during cycling, the half cell capacity at C/5 compared to C/20 increases from 9 $mAh\,g^{-1}$ to 29 $mAh\,g^{-1}$ after 314 cycles.

Figure 9 shows C/20 (see Figure 9a) and C/5 (see Figure 9b) voltage curves of the NaMn*HCF* half cell from Figure 8. The C/20 voltage curve from cycle 1 shows that NaMn*HCF* has only one voltage plateau, at 3.47 V vs. Na^+/Na during discharge and 3.54 V during charge (see Figure 9a). The initial charge capacity is 164.2 $mAh\,g^{-1}$ and agrees well with the theoretical capacity of 162.1 $mAh\,g^{-1}$ calculated in section 2.1.2.

With cycling, the voltage polarization increases and the plateau disappears continuously (see Figure 9a). This can be seen even more clearly in the C/5 cycles (see Figure 9b). This explains why the difference in half cell capacity between C/5 and C/20 increases significantly with cycle number, as seen in Figure 8.[37] As the polarization increases, the CV charge at the

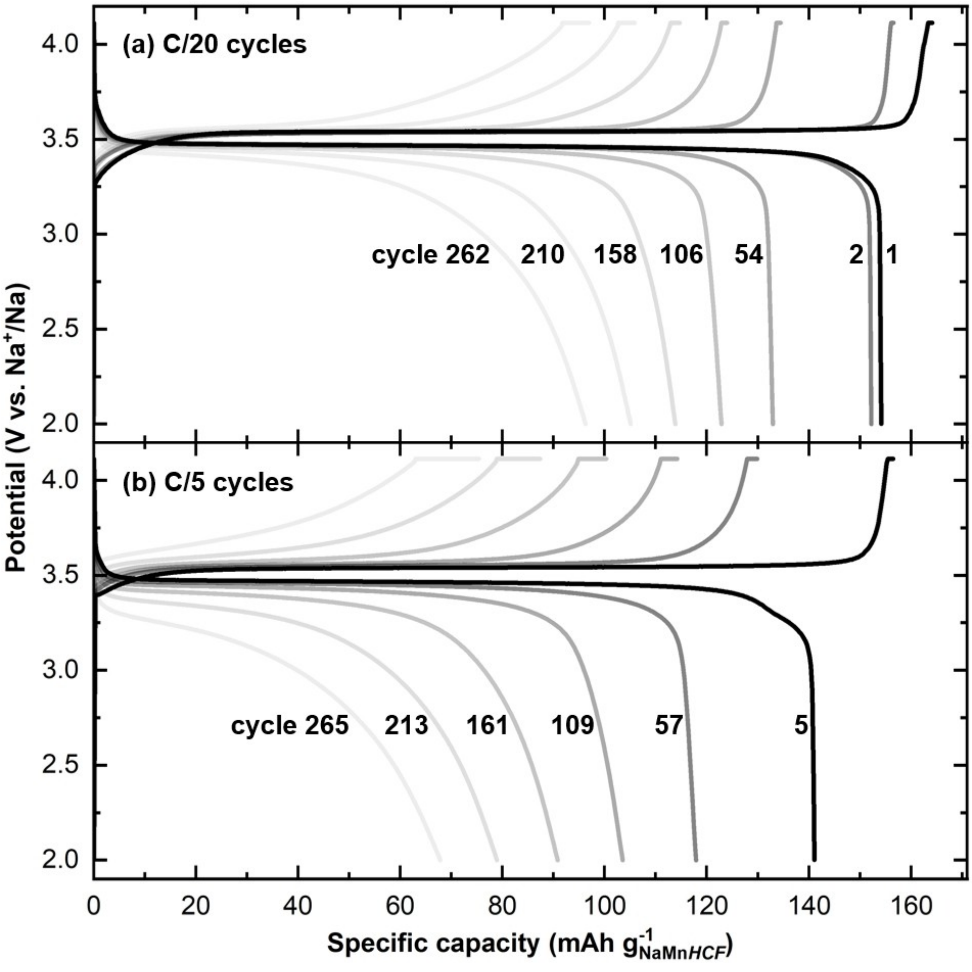

Figure 9. Potential curves of half cell with NaMn*HCF* cathode and sodium metal anode cycled from 2.0 to 4.1 V at 23 °C. 1 ᴍ $NaPF_6$ in PC + 5 wt% FEC was used as the electrolyte. After two initial C/20 cycles with a CV step to C/50 at the upper cut-off voltage, cycling continued at C/5 with a CV step to C/20. Every 50 C/5 cycles two C/20 check-up cycles were performed. Shown are the voltage curves of (a) the second C/20 check-up cycles and (b) ongoing C/5 cycles.

upper voltage limit increases in length (see Figure 9b). The voltage polarization for the initial C/20 and C/5 cycles shows no difference, indicating that the cell does not have a large initial internal resistance (compare cycle 1 from Figure 9a and cycle 5 from Figure 9b).

Figure 10 shows the C/20 (see Figure 10a) and C/5 (see Figure 10b) voltage curves of the NaMn*HCF*/HC full cell with $NaPF_6$ in EC:PC:DMC + FEC as the electrolyte from Figure 8. The initial charge capacity is 163.7 $mAh\,g^{-1}$ which agrees well with the half cell charge capacity and the theoretical value calculated in section 2.1.2. As with the other full cell electrolytes, the achieved initial discharge capacity of 139.4 $mAh\,g^{-1}$ leads to an initial coulombic efficiency (ICE) of 85.1 %. This initial capacity loss is due to irreversible Na^+-ion inventory loss at the HC anode like the SEI buildup. Since the positive and negative electrodes were balanced at a ratio of 1 : 1.2, there is a significant amount of HC excess, resulting in a low ICE.

Due to the voltage profile of HC, the full cells' voltage curves do not have a single plateau like the one seen in half cells. Instead, these full cells show a plateau up to about 60 $mAh\,g^{-1}$ at ~3.4 V during discharge before the slope of the HC voltage curve gradually decreases the full cell voltage (compare Figure 10a and Figure 9a).

In contrast to the voltage curves of the half cells, the voltage polarization hardly increases during cycling. Only the C/5 cycles show a small increase in polarization (see Figure 10b). As with the half cell in Figure 9, the voltage polarization for the initial C/20 and C/5 cycles shows no difference, indicating that the cell does not have a particularly high initial internal resistance.

2.2.2. Cycling in Narrow Voltage Window (2.5 – 3.65 V)

To investigate the influence of using a narrower voltage window, the NaMn*HCF*/HC cells were cycled between 2.5 and 3.65 V, which corresponds to the common voltage window used for commercial LFP/graphite cells.[38]

Figure 11a shows the cycling data for NaMn*HCF*/HC cells with either $NaPF_6$ in EC:DEC (see Figure 11a–1) or $NaPF_6$ EC:PC:DMC + FEC (see Figure 11a–2) as the electrolyte, which were cycled in a voltage window of 2.5 – 3.65 V (blank symbols). For

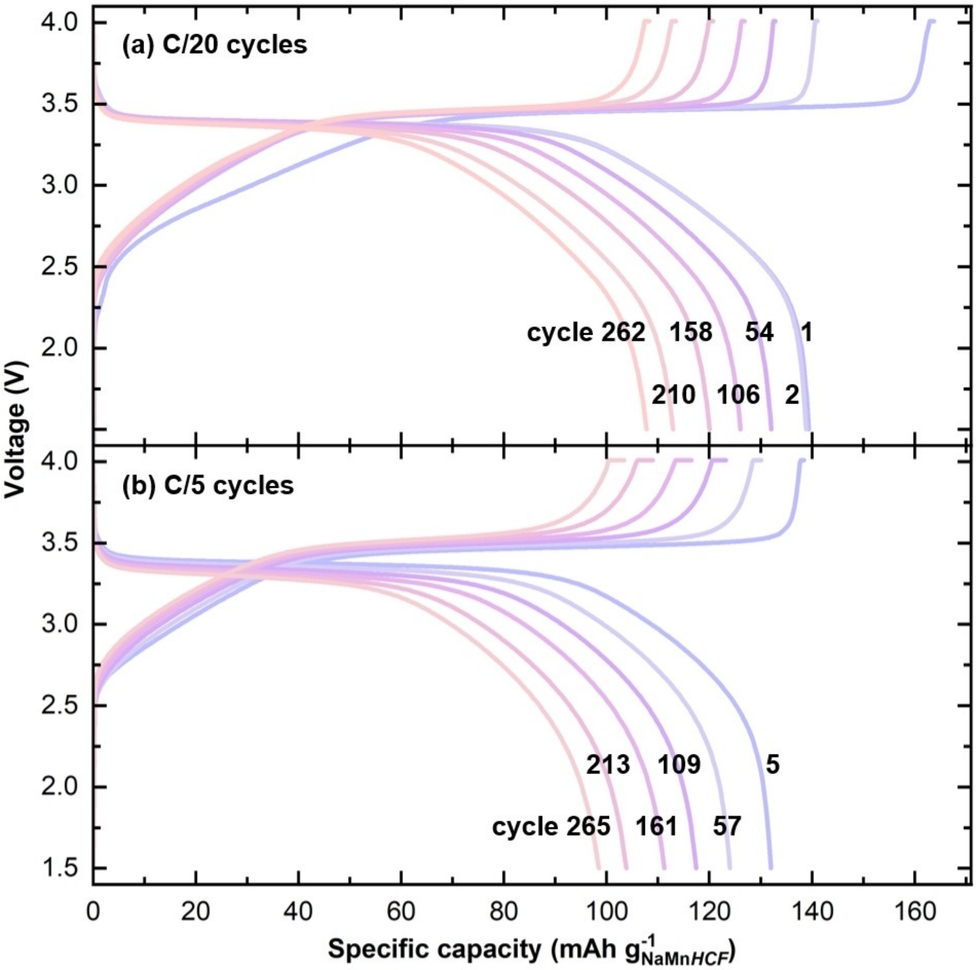

Figure 10. Voltage curves of full cell with NaMn*HCF* cathode and HC anode cycled from 1.5 to 4.0 V at 23 °C. 1 M $NaPF_6$ in a 1 : 1 : 1 volume ratio of EC:PC:DMC + 5 vol % FEC was used as the electrolyte. After two initial C/20 cycles with a CV step to C/50 at the upper cut-off voltage, cycling continued at C/5 with a CV step to C/20. Every 50 C/5 cycles two C/20 check-up cycles were performed. Shown are the voltage curves of (a) the second C/20 check-up cycles and (b) ongoing C/5 cycles.

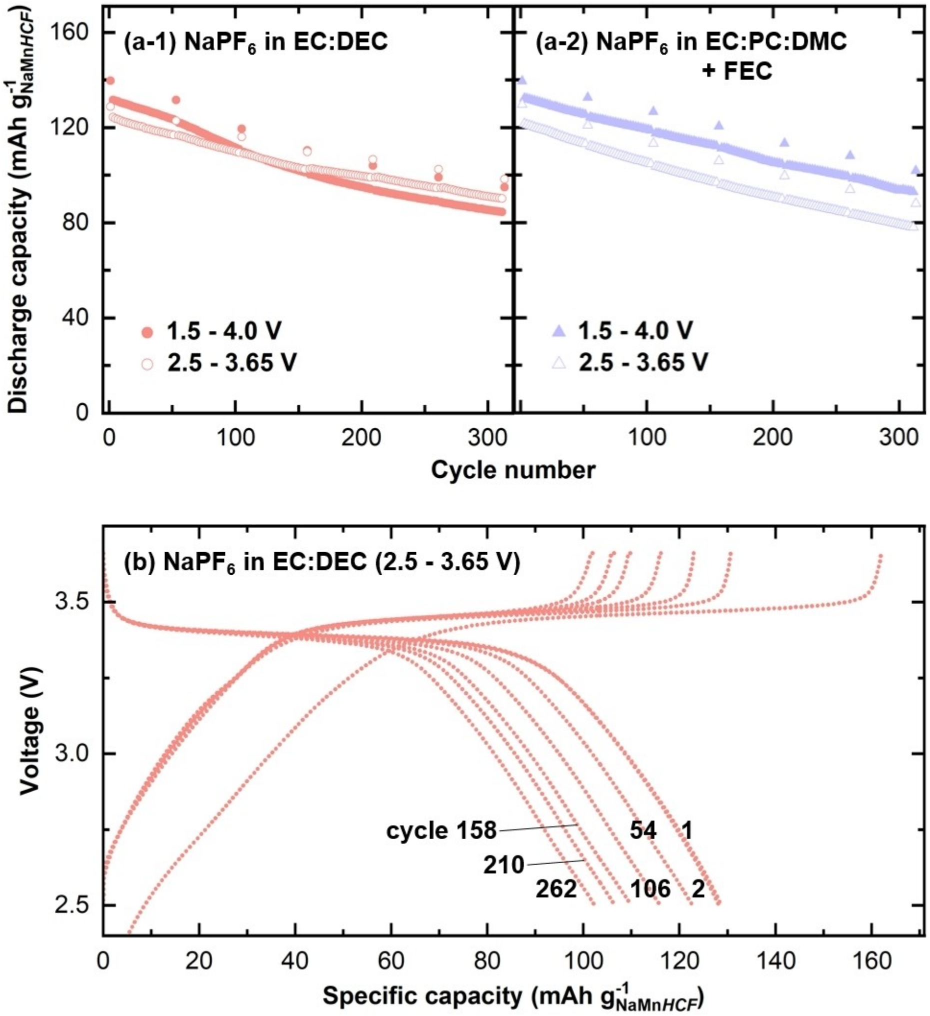

Figure 11. (a) Cycling data of full cells with NaMn*HCF* cathode and HC anode at 23 °C with either (a-1) $NaPF_6$ in EC:DEC or (a-2) $NaPF_6$ in EC:PC:DMC + FEC as the electrolyte. The cells were either cycled from 1.5 to 4.0 V (filled symbols) or from 2.5 to 3.65 V (blank symbols). After two initial C/20 cycles with a CV step to C/50 at the upper cut-off voltage, cycling continued at C/5 with a CV step to C/20. After every 50 cycles two C/20 check-up cycles were done. For a better visualization, only every second cycle is displayed. (b) Corresponding voltage curves of the second C/20 check-up cycles of $NaPF_6$ in EC:DEC cells cycled from 2.5 to 3.65 V.

reference, the cycling data for the 1.5 – 4.0 V voltage window from Figure 8 are also shown (filled symbols).

The initial discharge capacity of the cells with a narrowed voltage window is about 129 mAh g^{-1} and thus 10 mAh g^{-1} lower than for the voltage window of 1.5 to 4.0 V (compare Figure 11a and Figure 8). The initial discharge capacity for C/5 is also 10 mAh g^{-1} lower than that of the larger voltage window. The narrow voltage window affects the cycling stability of both tested cells. The $NaPF_6$ EC:DEC cell retains 98.3 mAh g^{-1} at C/20 which corresponds to 76.4 % of its initial capacity after 314 cycles. This is more than the 94.8 mAh g^{-1} and 67.9 % for the wider voltage window (see Figure 11a–1). The $NaPF_6$ EC:PC:DMC + FEC cell shows the opposite behavior. In the narrow voltage window, it retains 87.9 mAh g^{-1} (67.8 %) of its original C/20 capacity. This is less than in the wide voltage window, where it retains 101.7 mAh g^{-1} (72.9 %) of its original C/20 capacity.

Figure 11b shows the corresponding C/20 voltage curves of the $NaPF_6$ EC:DEC cell cycled from 2.5 to 3.65 V. The initial charge capacity is 162.3 mAh g^{-1}, which is consistent with the wide voltage window and therefore indicates that the charge is completed at 3.65 V. However, Figure 11b shows that discharge is not fully completed at 2.5 V, resulting in an ICE of only 79.3 % compared to the 85.1 % observed when cycling in the wider voltage window (compare cycle 1 of Figure 11b and Figure 10a). In addition to the irreversible Na^+-ion loss, this low value is due to Na^+-ions stuck remaining in the HC anode because the discharge is not completed at 2.5 V.

2.3. Post-Mortem Analyses

In this section, the NaMn*HCF*/HC coin cells presented in section 2.2 are disassembled and visually inspected. The post-mortem NaMn*HCF* cathodes are analyzed by SEM and XRD to investigate the structural degradation. They were also assembled into new half cells with a sodium metal anode and further cycled. That way, the loss of Na^+-ion inventory would be replenished and the contribution of Na^+-ion inventory consumption to the observed full cell capacity loss (see Figure 8 and 11) can be measured. The post-mortem HC anodes were analyzed by ICP-OES to quantify any Na, Mn and Fe which would have dissolved from the NaMn*HCF* and deposited on the anode.

*2.3.1. Visual Inspection of Disassembled NaMn*HCF*/HC Full Cells*

Figure 12 shows photographs of the post-mortem cathodes, separators and anodes from the coin cells that were cycled at C/5 with different electrolytes in different voltage windows for 314 cycles (see Figure 8 – 11). All electrodes stayed mechanically intact. None of the HC anodes show signs of sodium plating. The few visible scratches on the cathodes and anodes happened during cell disassembly. Interestingly, the $NaPF_6$ EC:DEC electrolyte turned light red, as can be seen from the coloration of the originally white separator (see Figure 12b). The $NaPF_6$ EC:DEC cell cycled from 1.5 to 4.0 V shows a stronger red color than the cell that was cycled from 2.5 to 3.65 V (compare Figure 12b–1 and b-2). The electrolyte used, which was stored in a sealed bottle, showed no discoloration with aging, which indicates that the coloration is triggered by a process within the cell. All other full cell electrolytes and therefore separators stayed colorless. The separator of the NaMn*HCF* half cell showed a gray coloration due to metallic sodium (see Figure 12a).

The post-mortem cathodes and anodes were used for further analyses.

*2.3.2. SEM of Post-Mortem NaMn*HCF *Cathodes*

Figure 13 shows SEM top-view images of the discharged post-mortem NaMn*HCF* cathodes after 314 C/5 cycles in a half cell and in full cells with HC using different electrolytes and different voltage windows shown in Figure 8 – 12. Additionally, Figure 13e shows a pristine NaMn*HCF* cathode after drying.

The cubic shaped particles of NaMn*HCF* are clearly visible. The smaller particles seen in the electrodes are C65 carbon black and the few fibres are vapor grown carbon fibres (VGCF), especially visible in Figure 13c–2.

All the post-mortem electrodes (Figure 13a-d), including the pristine electrode (Figure 13e), show cracks on the surface. They are not more pronounced in any specific cell configuration and are therefore most likely not the main reason for the difference in cell degradation seen in Figure 8 – 11. As can be seen in Figure 6, the cracks in the NaMn*HCF* particles already form during the initial drying step of the electrodes, but they appear to be less pronounced on the surface of the particles than in their core. The cross-sectional SEM images show stronger crack formation inside the particles (compare Figure 13 and 6).

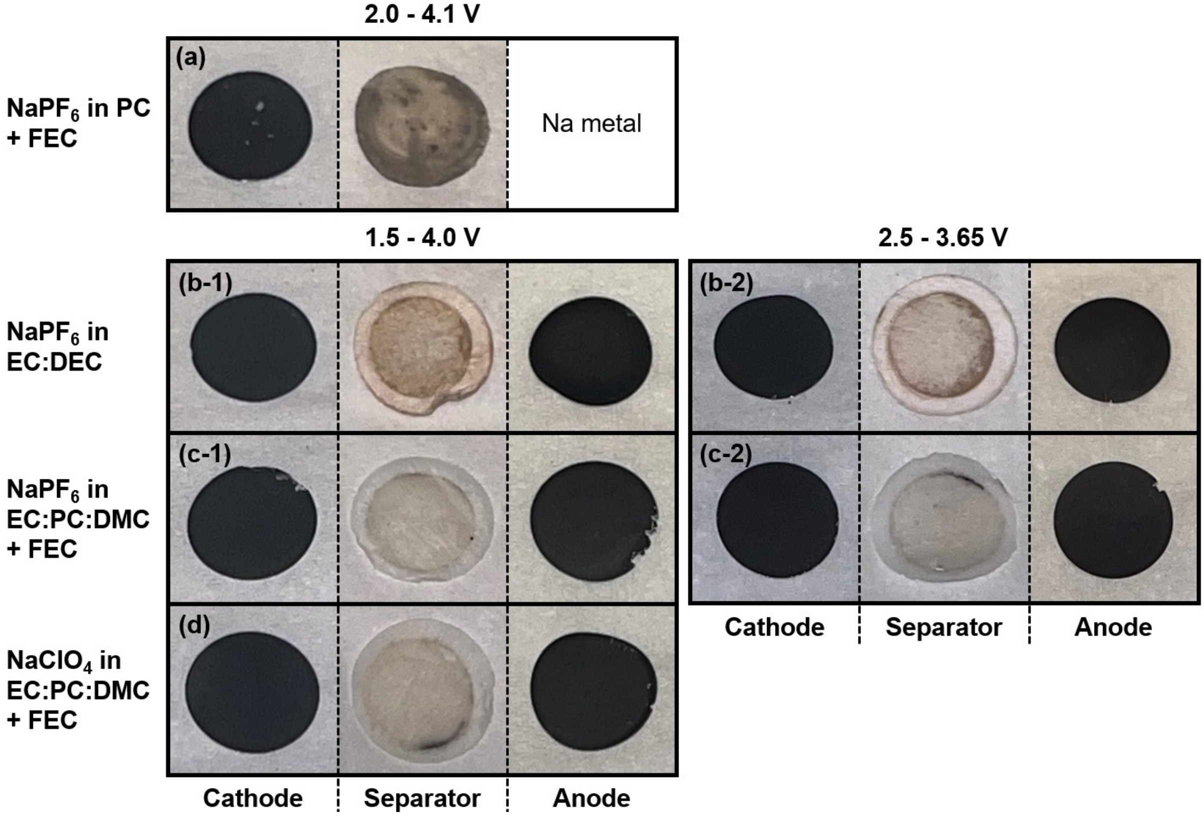

Figure 12. Photographs of discharged post-mortem coin cell cathodes, separators and anodes cycled with C/5 for 314 cycles with different electrolytes (shown in Figure 8–11). The half cell (a) was cycled from 2.0 to 4.1 V, the full cells were cycled from 1.5 to 4.0 V (b-1, c-1, d) or 2.5 to 3.65 V (b-2, c-2).

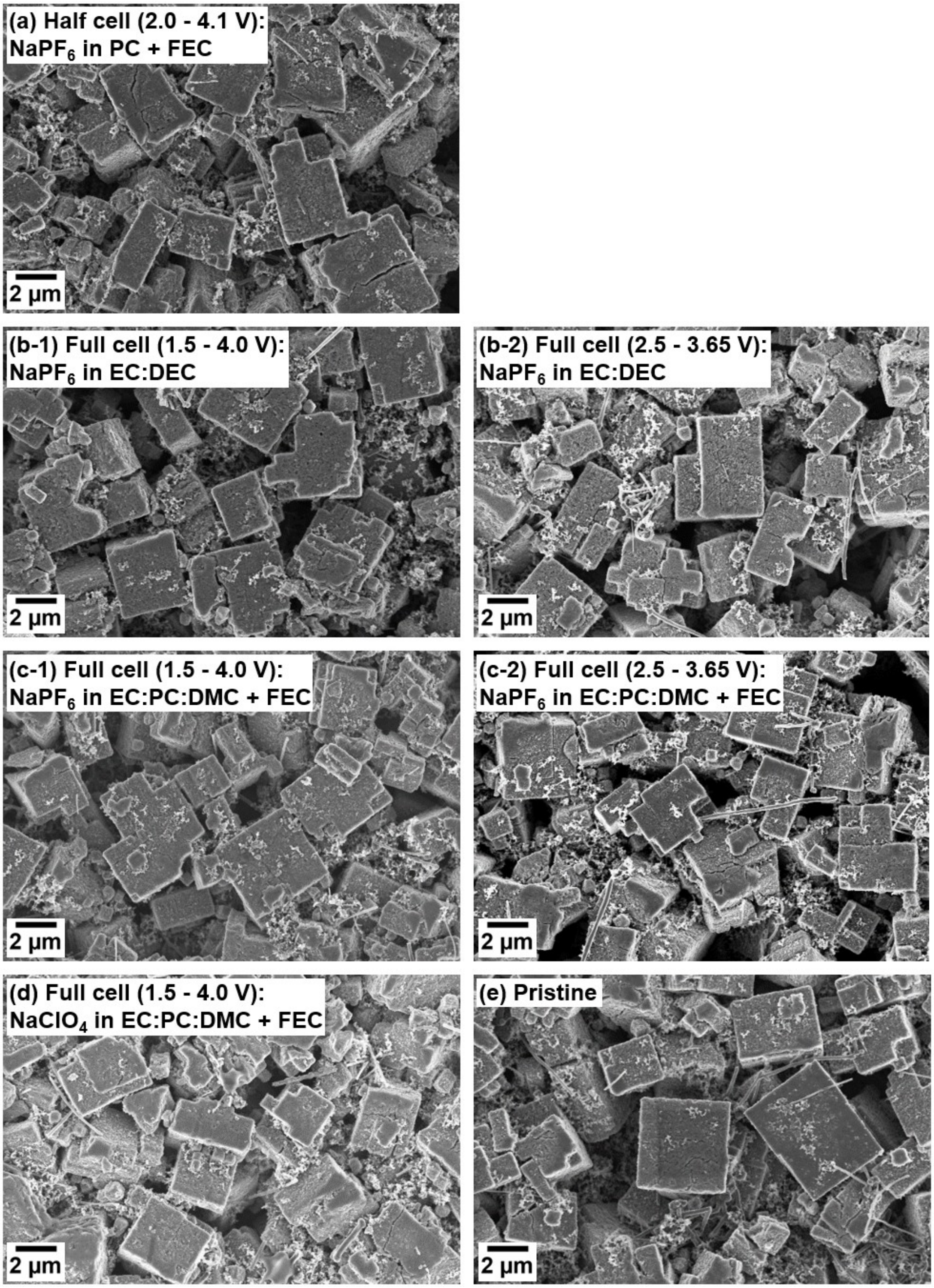

Figure 13. SEM images of the discharged post-mortem NaMn*HCF* cathodes from Figure 12 that were cycled with C/5 for 314 cycles with different electrolytes (shown in Figure 8 – 11). The half cell (a) was cycled from 2.0 to 4.1 V, the full cells were cycled from 1.5 to 4.0 V (b-1, c-1, d) or 2.5 to 3.65 V (b-2, c-2). In addition, a pristine cathode after drying is shown (e).

*2.3.3. XRD of Post-Mortem NaMn*HCF *Cathodes*

Figure 14 shows XRD patterns of discharged post-mortem NaMn*HCF* cathodes after 314 C/5 cycles in a half cell and in full cells with HC using different electrolytes and different voltage windows shown in Figure 8 – 13. Additionally, as a reference, Figure 14e shows the diffraction pattern of a pristine NaMn*HCF* cathode after drying. The XRD pattern of the post-mortem NaMn*HCF* half cell cathode shows the reflections of a cubic Fm-3 m material with severe peak broadening most likely due to

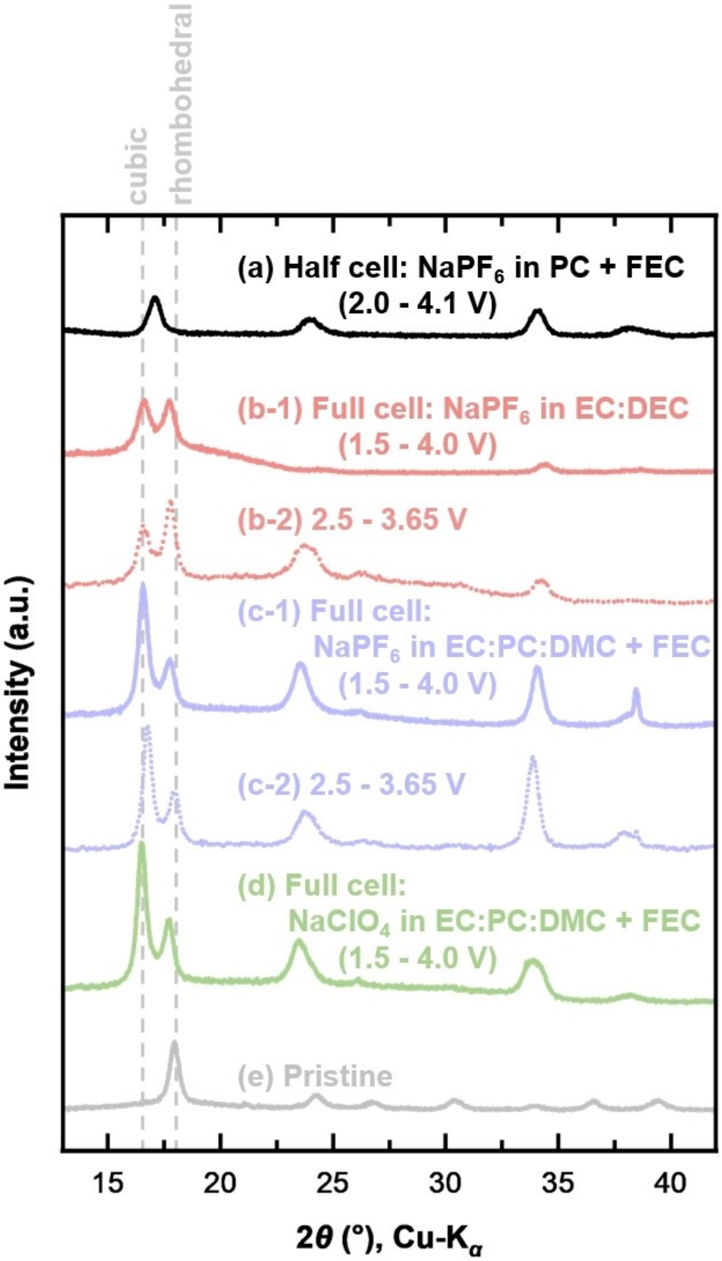

Figure 14. XRD of the discharged post-mortem NaMn*HCF* cathodes from Figure 12 that were cycled with C/5 for 314 cycles (shown in Figure 8 – 11). The half cell (a) was cycled from 2.0 to 4.1 V, the full cells were cycled from 1.5 to 4.0 V (b-1, c-1, d) or 2.5 to 3.65 V (b-2, c-2). In addition a pristine cathode after drying is shown (e).

micro-strain effects caused by the repeated phase transitions from the rhombohedral to the Na-poor cubic Prussian White structure that occurred during electrochemical cycling of the half cell (see Figure 14a).

The XRD patterns of the post-mortem NaMn*HCF* cathodes cycled with different electrolytes in full cells with HC all show contributions from a rhombohedral and cubic phase. The differentiation between cubic and monoclinc crystal symmetry is complicated by the severely broadened diffraction peaks, but it is unlikely that the monoclinic modification of NaMn*HCF* is present in these samples because it only occurs when it is fully sodiated and contains crystal water. The NaMn*HCF* electrodes were sufficiently dried to remove all crystal water before assembling the cells. Therefore, it makes sense that we see a mixture of rhombohedral and cubic crystal structures in the post-mortem full cell cathodes, as they experienced Na^+-ion loss. This is also consistent with the results of the in-situ XRD analysis of NaMn*HCF* half cells, described in the next section, where a phase transition from rhombohedral to cubic symmetry is observed. Compared to the NaMn*HCF* half cells the diffraction peaks of the cycled full cells exhibit less broadening indicating less severe structural degradation.

2.3.4. Half Cell Cycling of Post-mortem NaMnHCF Cathodes

In order to check whether the capacity loss of the NaMn*HCF*/HC full cells shown in Figure 8 and 11 is due to irreversible structural degradation or to the loss of Na^+-ion inventory, the NaMn*HCF* post-mortem cathodes were built into new half cells with sodium metal as the anode.

Figure 15a shows the cycling data of coin half cells that were built with the post-mortem NaMn*HCF* cathodes from Figure 12, which have previously undergone 314 C/5 cycles in a half cell or in full cells with a HC anode and different electrolytes (shown in Figure 8 – 11). The full cell cycling was carried out either from 1.5 to 4.0 V (filled symbols) or from 2.5 to 3.65 V (blank symbols). Due to problems with the galvanostatic cycler, some of the last cycles are missing.

Figure 15b shows the voltage curves of the first C/20 cycle of these half cells.

The post-mortem cathode, which was previously cycled from 2.5 to 3.65 V with the electrolyte $NaPF_6$ EC:PC:DMC + FEC, shows the highest discharge capacity of 130.8 mAh g^{-1} at the first C/20 discharge (see blank triangles, Figure 15a). It is followed by the $NaPF_6$ EC:DEC post-mortem cathode previously cycled from 2.5 to 3.65 V with a discharge capacity 116.7 mAh g^{-1} (empty circles) and the post-mortem cathodes previously cycled with $NaPF_6$ or $NaClO_4$ in EC:PC:DMC + FEC from 1.5 to 4.0 V with 115.4 and 118.5 mAh g^{-1}, respectively (see filled triangles and stars, Figure 15a). The $NaPF_6$ EC:DEC

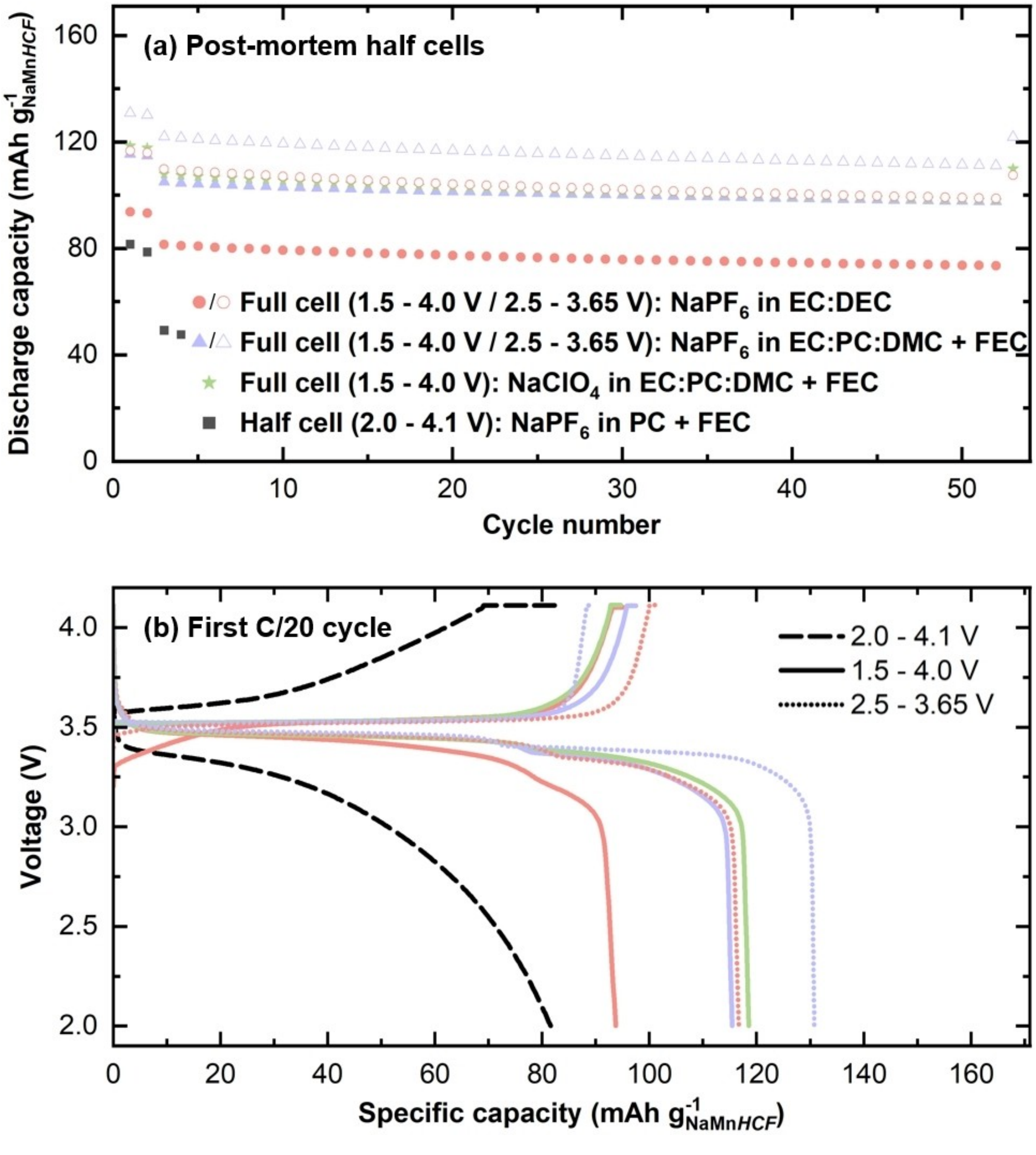

Figure 15. (a) Cycling data of half cells with post-mortem NaMn*HCF* cathodes shown in Figure 12, and sodium metal anode cycled from 2.0 to 4.1 V at 23 °C. 1 M $NaPF_6$ in PC + 5 wt% FEC was used as the electrolyte. After two initial C/20 cycles with a CV step to C/50 at the upper cut-off voltage, cycling continued at C/5 with a CV step to C/20. The post-mortem cathodes previously cycled 314 times at a C/5 rate with different electrolytes (shown in Figure 8 – 11) and were either cycled from 2.0 to 4.1 V in a half cell, or in full cells between 1.5 and 4.0 V (filled symbols) or 2.5 to 3.65 V (blank symbols). (b) Corresponding voltage curves of the first C/20 cycles.

post-mortem cathode, which was previously cycled from 1.5 to 4.0 V, showed the worst first C/20 discharge capacity of the full cell post-mortem cathodes with 93.7 mAh g^{-1} (see filled circles, Figure 15a). The post-mortem cathode, which was previously cycled in a half cell, has by far the worst capacity of all cases with only 81.5 mAh g^{-1} at the first C/20 discharge (see squares, Figure 15a).

Apart from the different initial capacities, all post-mortem full cell cathodes show similar cycling stability and retain between 92.1 and 93.2 % of their initial C/20 capacity after 53 cycles (see Figure 15a).

Looking at the coulombic efficiencies of the first C/20 cycles in Figure 15b, it can be seen whether the post-mortem cathodes used are as structurally degraded as Figs. 8 – 11 suggest, or whether the previously tested full cells show Na$^+$-ion inventory loss. To no surprise, the post-mortem cathode previously tested in a coin half cell shows a coulombic efficiency below 100 % in the first cycle, indicating that the post-mortem cathode is indeed degraded (see dashed line, Figure 15b). The NaPF$_6$ EC:DEC cathode, which was previously cycled from 1.5 to 4.0 V, also shows a coulombic efficiency below 100 %, which means that the cathode could not recover the capacity it lost when cycled in the full cell by replenishing the Na$^+$-ion inventory. Therefore, the NaMn*HCF* cathode must be degraded as much (see red solid line, Figure 15b). The other post-mortem cathodes of the full cells all have a coulombic efficiency above 100 %, which means that the capacity loss observed in the full cells (see Figure 8–11) is partly due to the degradation of the NaMn*HCF*, and partly to an irreversible loss of the Na$^+$-ion inventory. Interestingly, all post-mortem full cell cathodes show a voltage drop at about 80 – 90 mAh g^{-1} during discharge (see Figure 15b). The underlying reason for this phenomenon remains unclear at this time.

2.3.5. Na, Mn and Fe Content of Post-mortem HC Anodes

Feng *et al.* have already shown that the degradation of NaMn*HCF* may be due to the dissolution of Mn.[39] Therefore, the post-mortem HC anodes were examined for metal deposition.

Figure 16 shows the content of Na, Mn and Fe measured by ICP-OES in the discharged post-mortem HC anodes cycled either at 1.5 to 4.0 V (see Figure 16a) or at 2.5 to 3.65 V (see Figure 16b) for 314 C/5 cycles with different electrolytes (see Figure 8 – 12). The contents are given as percentage of the initial Na, Mn and Fe content in the NaMn*HCF* cathodes.

The amount of Na found in the post-mortem HC anodes is orders of magnitude higher than that of Mn and Fe. The NaPF$_6$ EC:DEC post-mortem anodes cycled from 1.5 to 4.0 V have the highest Na content of all cells at 19.27 % (see Figure 16a). The measured Na content is partly due to the initial irreversible Na loss. In addition, it can be assumed that further Na is trapped in the HC during cycling. This is slightly improved when the NaPF$_6$ EC:DEC cells are cycled only from 2.5 to 3.65 V leading to a Na content of 17.77 % (see Figure 16b).

The NaPF$_6$ EC:PC:DMC + FEC post-mortem anodes show Na contents of 12.12 % (1.5 – 4.0 V) and 15.97 % (2.5 – 3.65 V). This agrees well with the previous assumption that the discharge of the NaPF$_6$ EC:PC:DMC + FEC cells is not complete at 2.5 V, which is why many Na$^+$-ions are still stored in the HC and the Na content of the post-mortem anodes cycled from 2.5 to 3.65 V is higher than for the anodes cycled from 1.5 to 4.0 V. Interestingly the Na content of 12.12 and 10.41 % in the cells with EC:PC:DMC + FEC electrolytes (see Figure 16a) cycled from 1.5 to 4.0 V are below the initial coulombic inefficiency of around 15 % of those full cells (see cycle 1 in Figure 10a). This indicates that the first cycle capacity loss in the cells is not only due to the HC anode.

As for the Mn dissolution of NaMn*HCF* during cycling, this study was able to reproduce the observations made by Feng *et al.* A noticeable amount of 0.23 % (1.5 – 4.0 V) and 0.19 % (2.5 – 3.65 V) of the Mn was deposited on the HC anodes in the cells with a NaPF$_6$ EC:DEC electrolyte, as was also demonstrated by Feng *et al.*[39] Surprisingly, however, this Mn dissolution of NaMn*HCF* is suppressed when another electrolyte such as NaPF$_6$ or NaClO$_4$ in EC:PC:DMC + FEC is used. The reported Mn percentages of these two electrolytes were below the detection limit of the ICP-OES instrument and are therefore not meaningful.

Remarkably, all post-mortem HC anodes have a high Fe content between 0.37 – 0.72 %, with NaPF$_6$ EC:DEC again having the highest content. It is unknown whether this Fe content consists of dissolved Fe ions from the NaMn*HCF* cathode, whether they are complete $[Fe(CN)_6]^{4-}$ complexes or if the measured Fe content stems from the coin cell parts. More surprisingly, the Fe content of the NaPF$_6$ EC:PC:DMC + FEC electrolyte leads to a higher Fe content at the HC anode when the cell is cycled from 2.5 to 3.65 V instead of 1.5 to 4.0 V (0.54 vs. 0.39 %).

2.4. In-situ XRD

Figure 17 shows the in-situ XRD patterns of the second C/20 cycle of a NaMn*HCF* half cell that was cycled from 1.5 to 4.0 V. During the charging process, NaMn*HCF* initially exhibits a rhombohedral crystal structure. As Na$^+$-ions are extracted from the structure, it progressively transitions to a cubic crystal form. When fully charged and depleted of Na$^+$-ions, only cubic reflections are observed. In a full cell, however, fewer Na$^+$-ions are available compared to a half cell due to partial irreversible Na$^+$ consumption during formation. As a result, the before mentioned unit cell volume change is smaller in the full cell compared to the half cell, which could account for the poorer cycling performance observed in the half cell, as shown in Figure 8.

It is also worth mentioning that the NaMn*HCF* in full cells spends more time in the cubic than in the rhombohedral crystal structure, which could also have an effect on the cycling stability.

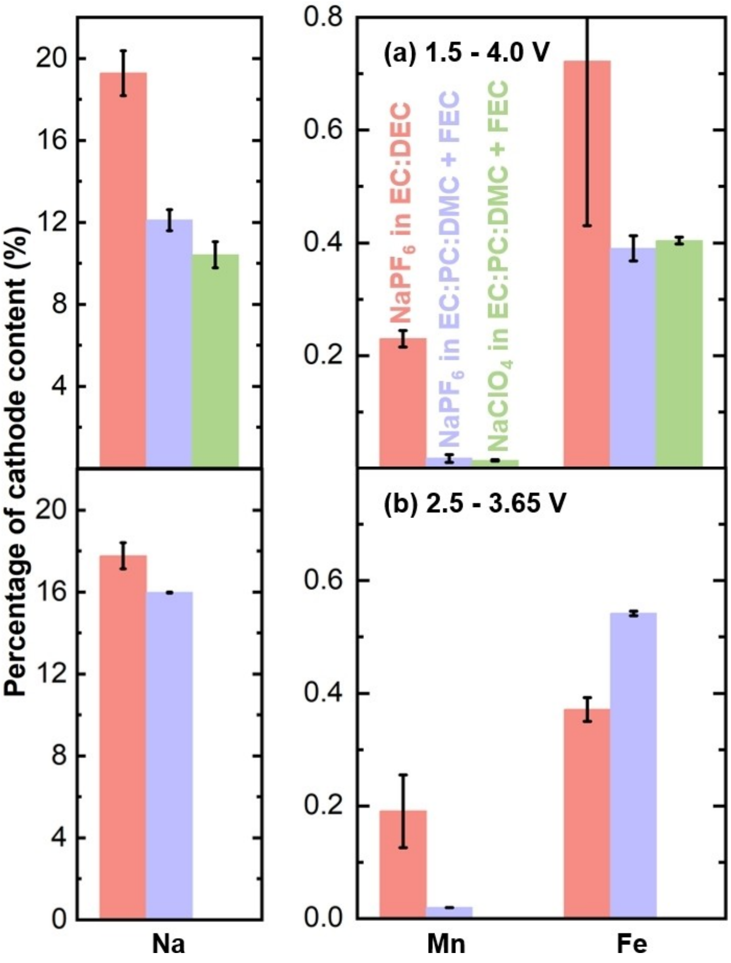

Figure 16. Na, Mn and Fe content in discharged post-mortem HC anodes from Figure 12 that have previously undergone 314 C/5 cycles in coin full cells with NaMn*HCF* cathodes with different electrolytes (shown in Figure 8 −11) and were either cycled from (a) 1.5 to 4.0 V or (b) 2.5 to 3.65 V. The contents are given as percentage of the initial Na, Mn and Fe content in the NaMn*HCF* cathodes. No full cells were tested with NaClO$_4$ in EC:PC:DMC + FEC from 2.5 to 3.65 V, so no green data is available in (b).

3. Discussion

3.1. Comparison of Full Cell Cycling Data with Post-mortem NaMn*HCF* Half Cells

Figure 18 summarizes the C/5 cycling data of the NaMn*HCF*/HC cells with different electrolytes shown in Figure 8, 11 and 15a, cycled from 1.5 to 4.0 V (see Figure 18a–1) and 2.5 to 3.65 V (see Figure 18b–1) and the corresponding post-mortem NaMn*HCF* half cell data (see Figs. 18a–2 and 18b–2). Additionally, a NaMn*HCF* half cell is shown (black squares) in Figure 18a.

It shows how much the NaMn*HCF* cathodes recover capacity when they are supplied with new Na$^+$-ions in the post-mortem half cells. As mentioned above, only the NaPF$_6$ EC:DEC full cell cycled from 1.5 to 4.0 V does not recover capacity, which means that the observed capacity loss is truly due to the NaMn*HCF* cathode degradation after 314 cycles (see circles in Figure 18a–1 and 18a–2). The other 1.5 – 4.0 V post-mortem cathodes recover between 13.8 and 22.2 mAh g^{-1} of capacity when built into new half cells. The capacity is recovered by new Na$^+$-ions from the sodium metal anode, which compensate for the Na$^+$-ion inventory loss during formation and cycling of the full cells.

The same behavior can be observed with the full cells that were only cycled from 2.5 to 3.65 V (see Figure 18b). In particular, the NaPF$_6$ EC:PC:DMC + FEC cell, recovers 42.9 mAh g^{-1} of capacity (compare triangles in Figure 18b–1 and 18b–2). This relatively large capacity gain is most likely also due to the fact that the full cell could not be completely discharged at a cut-off voltage of 2.5 V, which means that some Na$^+$-ions remained permanently intercalated in the HC. In the post-mortem half cell with a lower limiting voltage of 2.0 V, however, they were able to deintercalate from the HC.

3.2. NaMn*HCF* vs. LFP

As mentioned in the introduction, the entire cost advantage of SIBs may have to come from the cathode material. Therefore, it is important to consider the price of LFP compared to NaMn*HCF* per kWh. This section thus compares the specific energy of both technologies in half cells and full cells.

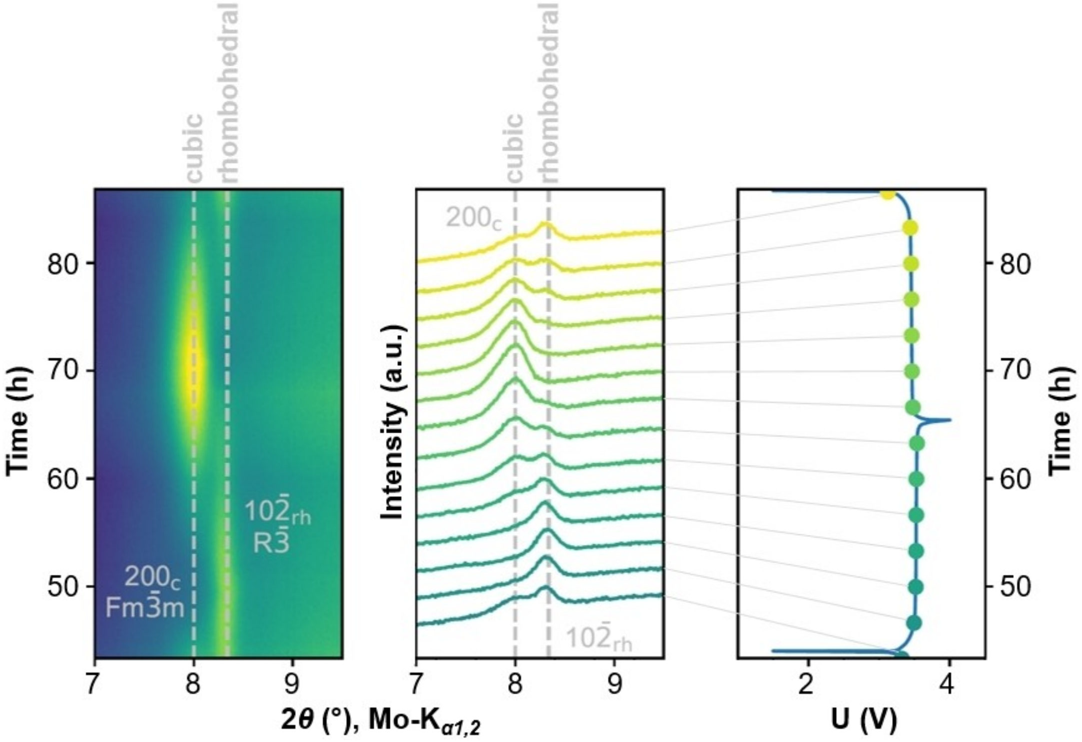

Figure 17. In-situ XRD contour plot of diffraction intensities recorded during the second C/20 cycle of a NaMn*HCF* half cell, cycled in the voltage window of 1.5 to 4.0 V.

3.2.1. Comparison of Half Cell Voltage Curves

Figure 19 shows the half cell voltage curves of the second C/20 cycle of NaMn*HCF* and commercial LFP. They show almost the same specific energy, with NaMn*HCF* having a slightly higher voltage plateau during discharge of 3.47 V for NaMn*HCF* versus 3.40 V for LFP. [40,41] Therefore, the cost comparison of NaMn*HCF* with LFP based on mass in Table 1 is valid.

3.2.2. Full Cell Comparison of NaMnHCF/HC and LFP/Graphite

Figure 20 shows a full cell comparison of the second C/20 voltage curves of NaMn*HCF*/HC cells cycled from either 1.5 to 4.0 V (solid purple line) or 2.5 to 3.65 V (dotted purple line) and commercial LFP/graphite (dotted yellow line). In addition to the specific capacity based on the cathode materials, Figure 20 also shows the specific capacity based on the anode materials HC and graphite. Note that those values were calculated by assuming a capacity of 335 mAh g^{-1} for the HC and 370 mAh g^{-1} for the graphite and an N:P ratio of 1.2.

Based on the cathode active material the LFP/graphite cell demonstrates a discharge capacity of 125.8 mAh g^{-1}, while NaMn*HCF*/HC cells exhibit 138.8 mAh g^{-1} and 128.8 mAh g^{-1} when cycled within 1.5–4.0 V and 2.5–3.65 V ranges respectively. The HC's specific capacity is slightly lower, measuring 260 mAh g^{-1} (1.5 – 4.0 V) and 240 mAh g^{-1} (2.5–3.65 V), compared to 250 mAh g^{-1} for graphite, assuming an N:P ratio of 1.2.

NaMn*HCF*/HC cells deliver an average discharge voltage of 3.21 V (1.5 – 4.0 V) and 3.26 V (2.5 – 3.65 V). The specific energy of NaMn*HCF*/HC cycled from 1.5 to 4.0 V, based solely on active materials, reaches 289 Wh kg^{-1} in the second C/20 cycle comparable to LFP/graphite at approximately 312 Wh kg^{-1}.

Despite its competitive specific energy, NaMn*HCF*/HC lags behind LFP/graphite in terms of cycle life, requiring further optimization. Industrial-scale improvements are also needed, such as increasing the areal loading of NaMn*HCF* cathodes from 1 mAh cm^{-2} to the standard 2 – 3.5 mAh cm^{-2}, along with boosting the active material content from 88 wt%.

One significant limitation of NaMn*HCF* compared to LFP is its lower energy density (Wh L^{-1}). NaMn*HCF*, like other Prussian White analogues, exhibits a crystal density of approximately 2.05 kg L^{-1}, while LFP has a considerably higher crystal density of around 3.35 kg L^{-1}.[42] This difference implies that LFP requires approximately 39% less volume to store the same amount of energy at the crystal level. Consequently, NaMn*HCF* must compensate for this volumetric disadvantage at the electrode level by optimizing the electrode structure. One approach is to utilize larger particles, which can increase the tap density.

In contrast to LFP, which suffers from poor electronic conductivity and thus requires either smaller particles or the addition of substantial amounts of carbon additives, NaMn*HCF* may have an advantage in this area due to its potential to accommodate larger particles without such significant compromises.

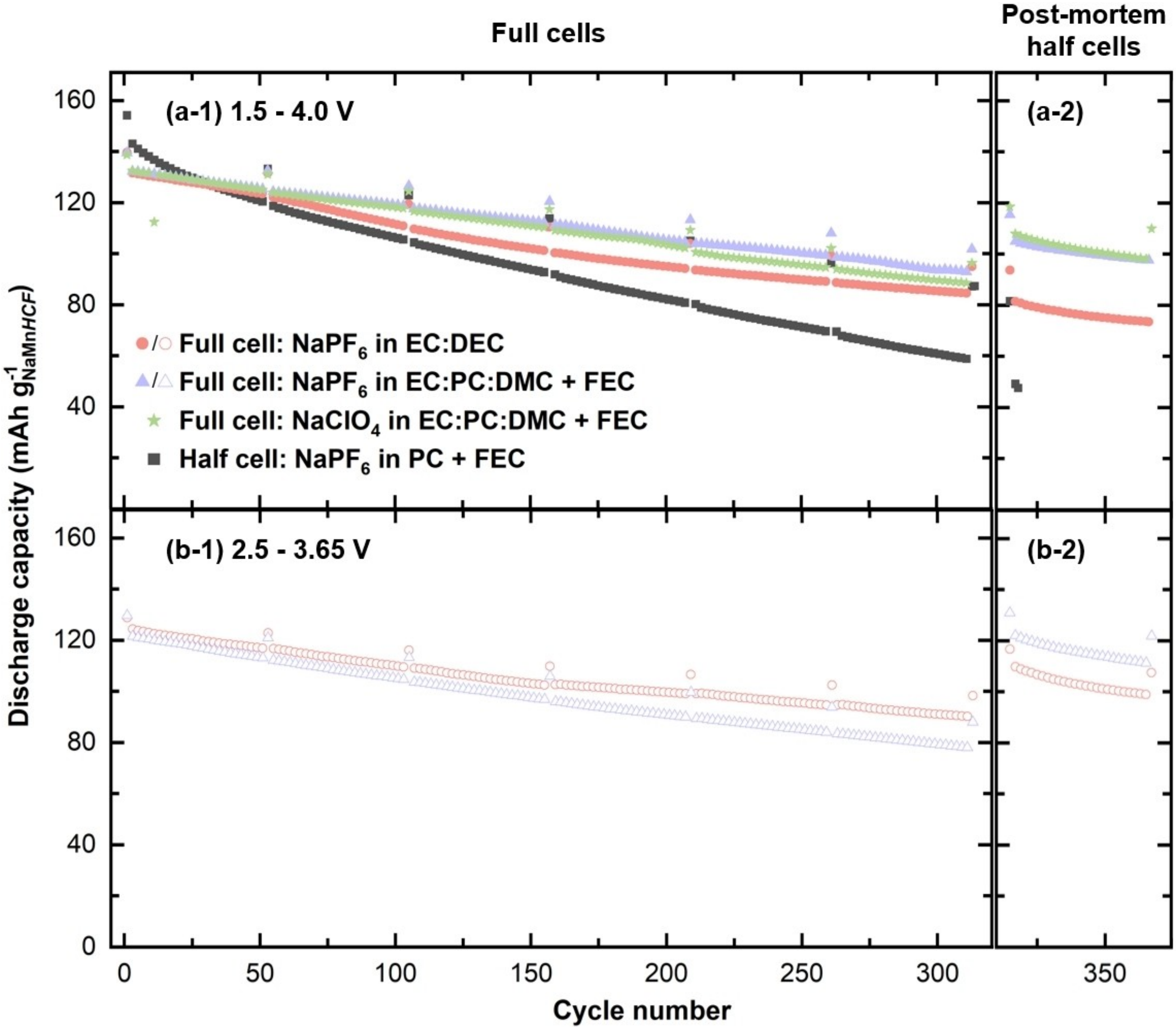

Figure 18. Cycling data of full cells with NaMn*HCF* cathode and HC anode cycled from (a-1) 1.5 to 4.0 V or (b-1) 2.5 to 3.65 V with different electrolytes. After 314 full cell cycles, the post-mortem cathodes were cycled in half cells with a sodium metal anode from 2.0 to 4.1 V (a-2, b-2). Additionally the black squares show a NaMn*HCF* cathode cycled in a coin half cell with a sodium metal anode from the beginning. The cycling was done at 23 °C and consisted of two initial C/20 cycles with a CV step to C/50 at the upper cut-off voltage before the cycling continued at C/5 with a CV step to C/20. After every 50 cycles two C/20 check-up cycles were done. For a better visualization, only every second cycle is displayed.

The density difference between graphite and HC is less pronounced, at 2.26 kg L^{-1} and 2.06 kg L^{-1}, respectively, further influencing the material selection and design for energy storage systems.[42]

4. Conclusions

- This study provides a framework for the characterization of NaMn*HCF* as a cathode material in SIBs and investigates the effects of $[Fe(CN)_6]^{4-}$ vacancies on the material properties. In addition, it was shown that effective removal of crystal water can be achieved with relatively low drying temperatures $<100\,^{\circ}C$ in combination with a high vacuum.
- NaMn*HCF* cathodes with 88 wt% active material and a surface loading of approximately 1 mAh cm^{-2} were prepared with a water-based slurry, paired with hard carbon anodes and tested in coin cells. Cycling stability varied with the choice of electrolyte, with the most stable electrolyte retaining 72.9 % of its original capacity after 314 cycles at C/5. Cells cycled from 2.5 to 3.65 V showed compatibility of this chemistry with the standard LFP/graphite voltage window, with an initial capacity deficit of approximately 10 mAh g^{-1}.
- Surprisingly, post-mortem ICP-OES analyses of the HC anodes showed that the Mn dissolution in NaMn*HCF* often quoted in literature is negligible when a suitable electrolyte is chosen. Additional half-cell cycling of post-mortem NaMn*HCF* cathodes showed that the capacity loss of the full cells was due to both NaMn*HCF* degradation and Na$^+$-ion inventory loss. After excluding Mn dissolution as a frequently cited explanation for the main degradation, further studies are needed to explain the observed cycling behavior of the half and full cells with different electrolytes.
- When comparing NaMn*HCF*/HC with LFP/graphite, the specific energy (Wh kg^{-1}) of both chemistries was found to be comparable. However, NaMn*HCF*'s lower crystal density

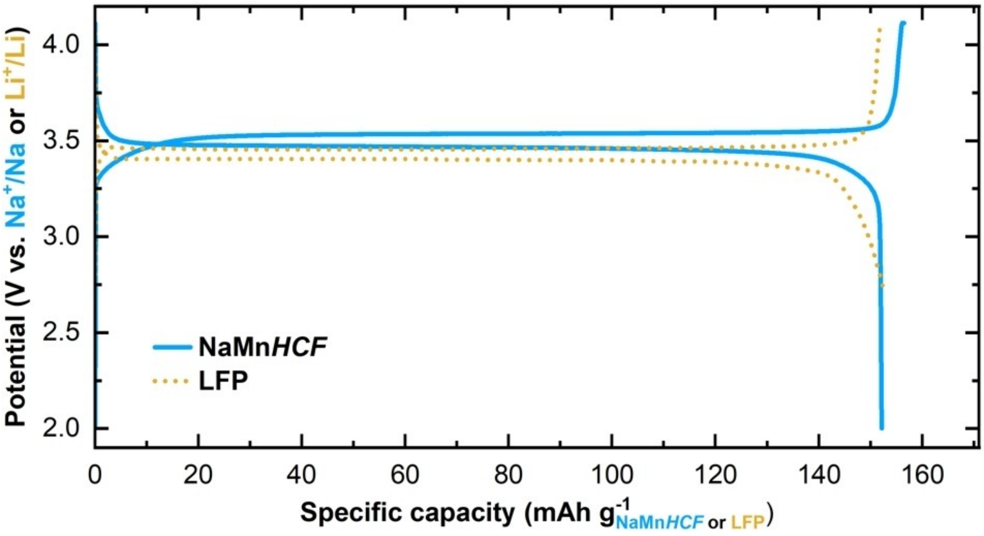

Figure 19. Second C/20 cycle of half cells with NaMn*HCF* cathode and a sodium metal anode (solid blue line) cycled from 2.0 to 4.1 V or LFP cathode and a lithium metal anode (dotted orange line) cycled from 2.7 to 4.1 V. LFP data used from Rowden *et al.*[40]

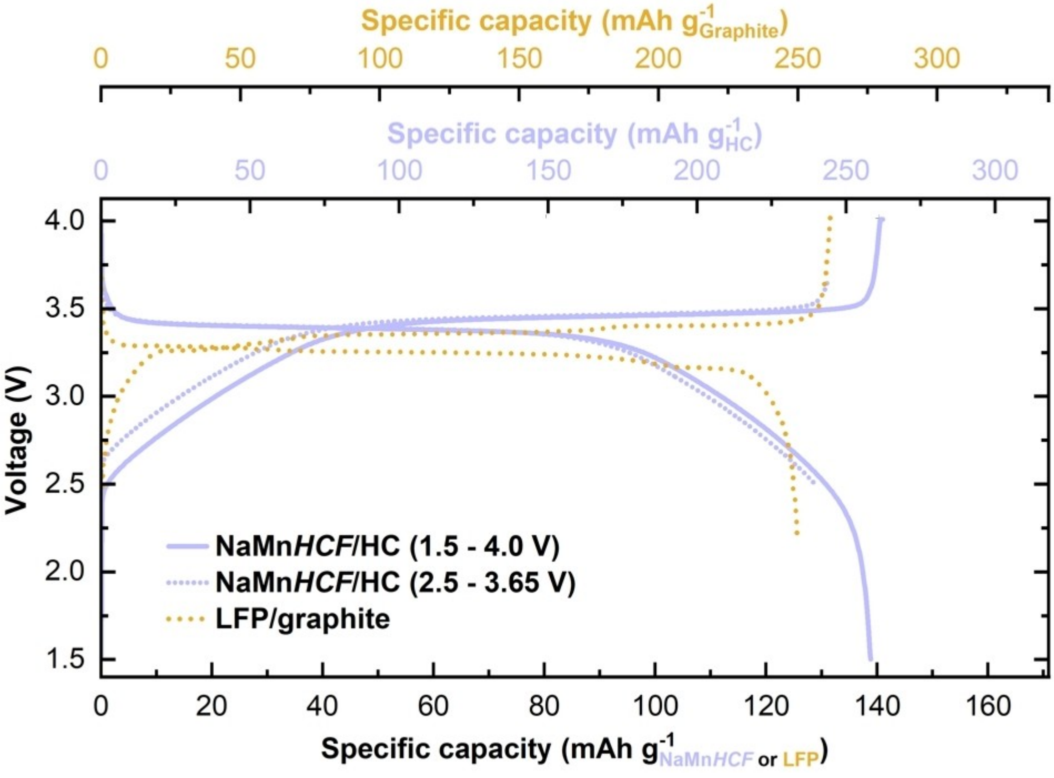

Figure 20. Second C/20 cycle of full cells with NaMn*HCF* cathode and HC anode cycled from 1.5 to 4.0 V (solid purple line) or 2.5 to 3.65 V (dotted purple line) or a LFP cathode and a graphite anode (dotted orange line) cycled from 2.2 to 4.1 V. LFP/graphite data used from Rowden *et al.*[40] For comparison the specific capacity of HC and graphite were calculated by using an N:P ratio of 1.2 when in reality the LFP/graphite data had a ratio of 1.1.

reduces its volumetric energy density (Wh L^{-1}) relative to LFP, underscoring a key area for improvement in NaMn*HCF* performance.

Experimental Section

Positive electrode material: The NaMn*HCF* was synthesized in a 50 L tank reactor by a modified coprecipitation method described in Xu *et al.*[25] $Na_4Fe(CN)_6$, $MnSO_4$ and $Na_3C_6H_5O_7$ dissolved in deionized water were mixed in the 50 L tank reactor with vigorous stirring at 50 °C. The collected product was filtered and washed three times with deionized water. It was then dried for 24 hours at 60 °C under vacuum <20 mbar.

Scanning electron microscope (SEM): The SEM images were taken with a Zeiss Supra 55. The NaMn*HCF* powder sample was prepared by adhering the powder on carbon paint. The NaMn*HCF* electrode cross-sections were prepared using a broad ion beam slope cutting (BIBSC) technique to produce smooth surfaces.

Particle size distribution (PSD) and specific surface area: The particle size distribution of the NaMn*HCF* powder was determined by dispersing the sample in 2-propanol and measuring the particles' size by laser scattering in a Horiba LA950 (Retsch Technology). The specific surface area was measured with a Gemini VII2390a (NSA, Micromeritics) and calculated using the BET method.

Inductively coupled plasma optical emission spectroscopy (ICP-OES): The chemical composition of the NaMn*HCF* powder was determined by ICP-OES. (iCAP 7600 Duo, Thermo Fisher Scientific). About 10 mg of the samples (weighing accuracy ± 0.06 mg) were dissolved in 25 ml hydrochloric acid at 80 °C for 4 h in a graphite oven (EasyDigest, Analab).

For the post-mortem analysis of the HC anodes about 10 mg of the samples (with aluminum current collector, weighing accuracy ± 0.06 mg) were extracted in 6 ml hydrochloric acid and 2 ml nitric acid at 80 °C for 2 h in the graphite oven, then for 2 h in an ultrasonic bath and again for 12 h at 80 °C in the graphite oven.

The analysis of the elements Na, Mn and Fe was conducted with four different calibration solutions and an internal standard (Sc). The range of the calibration solutions did not exceed a decade. The three major wavelengths of the elements have been used for calculation.

Mössbauer spectroscopy: ^{57}Fe Mössbauer spectroscopy of NaMn*HCF* was performed in transmission mode at room temperature on a constant-acceleration spectrometer (WissEl) with a ^{57}Co(Rh) source. The samples were sealed inside polyethylene/aluminum bags in an Ar-filled glovebox and the mass was about 20 mg cm^{-2}. The spectra were fitted with WinNormos. All isomer shifts are given relative to that of α-Fe metal.

X-ray diffraction (XRD): XRD was performed on NaMn*HCF* powder and electrodes sealed in a Bruker Airtight Specimen Holder in an Ar-filled glovebox and measured using a Bruker D2 Bragg-Brentano diffractometer with Cu-K_α radiation. The scattering angle (2θ) ranged from 10 to 70° and was increased in steps of 0.02° per second.

Thermogravimetric analysis (TGA): The TGA was performed with a STA 449 F3 Jupiter (Netzsch Gerätebau) on NaMn*HCF* powder that was either pristine or dried for 15 h at 150 °C and $3\cdot10^{-3}$ mbar. The powders were heated from 25 to 1,000 °C at 5 K min^{-1} in an Ar atmosphere.

Electrode preparation: H_2O-based positive electrodes were made from NaMn*HCF* mixed with C65 carbon black (Timcal C-NERGY Super C65, Imerys, Switzerland), VGCF (VGCF–H, Resonac, Japan) and poly(acrylic acid) (PAA) binder with an average molecular weight of 450 000 g mol^{-1} (Sigma-Aldrich, USA) at a weight ratio of 88:4:2:6 and a solid content of 40 wt%. The PAA was first neutralized to 75% with NaOH. The NaMn*HCF* powder was previously dried for 15 h at 150 °C and $3\cdot10^{-3}$ mbar and weighed in an Ar-filled glovebox to ensure that no residual water is measured with the powder awhich could falsify the solids ratio. The positive electrode slurry was coated onto an aluminum foil using a doctor blade with a 200 μm gap. After drying at room temperature, the electrode was calandered at 10 N/mm in a Sumet-Messtechnik laboratory calander. H_2O-based negative electrodes were made from HC (Kuranode, Type II, 9 μm, Kuraray, Japan) mixed with C65 carbon black, carboxymethyl cellulose (CMC, MAC500LC, Nippon Paper, Japan) and styrene-butadiene rubber (SBR, BM-4xx, Zeon, Japan) binder at a weight ratio of 93:1.4:1.87:3.73. The negative electrode slurry was also applied to an aluminum foil and calandered after drying. Further details on the fabrication of the negative electrode can be found in Stüble *et al.* and Müller *et al.*[43,44] Electrode disks with a diameter of 12 mm for the positive and negative electrodes were punched and dried for 15 h at 130 °C and $<3\cdot10^{-3}$ mbar before cell assembly. After drying, the positive active material loading was 6.7 mg cm^{-2} (0.9 mAh cm^{-2} for a capacity of 150 mAh g^{-1}) and the negative active material loading was 3.7 mg cm^{-2} (1.1 mAh cm^{-2} for a capacity of 335 mAh g^{-1}), resulting in a N/P ratio of 1.2.

Electrolyte preparation: Five different electrolytes are used in this work. Half cells used 1 M $NaPF_6$ (Chemfish Tokyo, Japan) in PC and 5 wt% FEC. Full cells used 1 M $NaPF_6$ either in a 3:7 volume ratio of EC and DEC or in a 1:1:1 volume ratio of EC, PC and DMC plus 5 vol% FEC. In addition, 1 M $NaClO_4$ (Alfa Aesar, USA) in a 1:1:1 volume ratio of EC:PC:DMC with 5 vol% FEC was used for full cells. All solvents are from Gotion, Fremont, USA. All electrolyte components were used as received and mixed in an Ar-filled glovebox.

Coin cell assembly: 2032-type coin half cells were assembled using a 12 mm diameter NaMn*HCF* cathode and a 13 mm diameter negative sodium metal electrode with a glass fiber separator (Whatman GF/C, 260 μm thickness, UK) in between. The coin full cells were assembled using a 12 mm diameter NaMn*HCF* electrode and a 12 mm diameter HC electrode with a glass fiber separator in between. The full cells were balanced in a N/P ratio of 1.2, meaning that the HC anode had 20% more capacity than the NaMn*HCF* cathode. 200 μL of electrolyte was used for each cell. Each cell configuration was built twice.

Electrochemical testing: Galvanostatic cycling is carried out in a temperature-controlled chamber at 23 °C. After two initial C/20 cycles (1 C $=$ 150 mA g^{-1} NaMn*HCF*) with a CV step to C/50 at the upper cut-off voltage, cycling continued at C/5 with a CV step to C/20 at the upper cut-off voltage. After every 50 cycles, two C/20 check-up cycles were done. The half cells were cycled from 2.0 to 4.1 V and the full cells either from 1.5 to 4.0 V or 2.5 to 3.65 V.

In-situ XRD:

In-situ XRD measurements were done on a laboratory diffractometer for battery research with Mo-$K_{\alpha1,2}$ radiation.[45] The diffractometer is equipped with a Dectris Eiger 4 MW CdTe detector. Detector calibration was done with a LaB_6 (NIST standard 660c) reference material. Diffraction patterns were collected with an exposure time of 10 min on coin cells with glass windows which were cycled at C/20.

Coin cell disassembly for post-mortem tests: After the cells had completed 314 cycles and discharged to their lower cut-off voltage, they were opened in an Ar-filled glovebox. The NaMn*HCF* cathodes and HC anodes were separated and washed in DMC overnight. Since there were two cells for each cell configuration, one NaMn*HCF* cathode was assembled and re-used in a new half cell and the other was analyzed with XRD and SEM. The HC anodes were used for ICP-OES measurements.

Acknowledgements

The authors thankfully acknowledged the support of Monika Raab (Institute for Applied Materials – Energy Storage Systems, Karlsruhe Institute of Technology) for PSD, BET and TGA measurements, Dr. Andreas Hofmann (Institute for Applied Materials – Materials Science and Engineering, Karlsruhe Institute of Technology) for the electrolyte preparation and Julian Klemens (Thin Film Technology, Karlsruhe Institute of Technology) for the HC anode coating.

This work contributes to research performed at CELEST (Center for Electrochemical Energy Storage Ulm – Karlsruhe) and at the Post-Lithium Storage (POLiS) Cluster of Excellence, which was funded by the German Research Foundation (DFG) under Project ID 390874152. Open Access funding enabled and organized by Projekt DEAL.

Conflict of Interests

The authors declare no conflict of interest.

Data Availability Statement

The data that support the findings of this study are openly available in zenodo at http://doi.org/10.5281/zenodo.14359482.

Keywords: sodium-ion batteries · Prussian White · Prussian Blue

[1] G. Callaway, C. Ding, I. Fitzgibbon, H. Gregor, M. N. Malik and M. Smith, Could supply-chain issues derail the energy transition?, https://www.mckinsey.com/industries/oil-and-gas/our-insights/could-supply-chain-issues-derail-the-energy-transition#/.
[2] D. A. Stevens and J. R. Dahn, *J. Electrochem. Soc.* **2000**, *147*, 1271.
[3] A. Adamson, R. Väli, M. Paalo, J. Aruväli, M. Koppel, R. Palm, E. Härk, J. Nerut, T. Romann, E. Lust and A. Jänes, *RSC Adv.* **2020**, *10*, 20145–20154.
[4] D. Igarashi, Y. Tanaka, K. Kubota, R. Tatara, H. Maejima, T. Hosaka and S. Komaba, *Adv. Energy Mater.* **2023**, *13*, 1–11.
[5] J. F. Peters, M. Baumann, J. R. Binder and M. Weil, *Sustain. Energy Fuels* **2021**, *5*, 6414–6429.
[6] Q. Tao, H. Ding, X. Tang, K. Zhang, J. Teng, H. Zhao and J. Li, *Energy Fuels* **2023**, *37*, 6230–6239.
[7] M. Häringer, H. Geßwein, N. Bohn, H. Ehrenberg and J. R. Binder, *ChemElectroChem* DOI:10.1002/celc.202300401.
[8] G. Yan, S. Mariyappan, G. Rousse, Q. Jacquet, M. Deschamps, R. David, B. Mirvaux, J. W. Freeland and J. M. Tarascon, *Nat. Commun.* DOI:10.1038/s41467-019-08359-y.
[9] M. He, A. El Mejdoubi, D. Chartouni, M. Morcrette, P. Troendle and R. Castiglioni, *J. Power Sources* **2023**, *588*, 233741.
[10] M. Schmidt, V. Mereacre, H. Geßwein, N. Bohn, S. Indris and J. R. Binder, *Adv. Energy Mater.* DOI:10.1002/aenm.202301854.
[11] L. Zhang, J. Deshmukh, H. Hijazi, Z. Ye, M. B. Johnson, A. George, J. R. Dahn and M. Metzger, *J. Electrochem. Soc.* **2023**, *170*, 070514.
[12] Y. Li, Q. Zhou, S. Weng, F. Ding, X. Qi, J. Lu, Y. Li, X. Zhang, X. Rong, Y. Lu, X. Wang, R. Xiao, H. Li, X. Huang, L. Chen and Y. S. Hu, *Nat. Energy* **2022**, *7*, 511–519.
[13] A. Kraft, *Ionics* **2021**, *27*, 2289–2305.
[14] H. Wewetzer, Ein Medikament gegen Cäsium, https://www.handelsblatt.com/technik/medizin/entgiftung-ein-medikament-gegen-caesium/3980270.html.
[15] Y. Lu, L. Wang, J. Cheng and J. B. Goodenough, *Chem. Commun.* **2012**, *48*, 6544–6546.
[16] J. Song, L. Wang, Y. Lu, J. Liu, B. Guo, P. Xiao, J. J. Lee, X. Q. Yang, G. Henkelman and J. B. Goodenough, *J. Am. Chem. Soc.* **2015**, *137*, 2658–2664.
[17] L. Wang, J. Song, R. Qiao, L. A. Wray, M. A. Hossain, Y. De Chuang, W. Yang, Y. Lu, D. Evans, J. J. Lee, S. Vail, X. Zhao, M. Nishijima, S. Kakimoto and J. B. Goodenough, *J. Am. Chem. Soc.* **2015**, *137*, 2548–2554.
[18] M. Pasta, C. D. Wessells, N. Liu, J. Nelson, M. T. McDowell, R. A. Huggins, M. F. Toney and Y. Cui, *Nat. Commun.* **2014**, *5*, 1–9.
[19] W. R. Brant, R. Mogensen, S. Colbin, D. O. Ojwang, S. Schmid, L. Häggström, T. Ericsson, A. Jaworski, A. J. Pell and R. Younesi, *Chem. Mater.* **2019**, *31*, 7203–7211.
[20] K. Chayambuka, G. Mulder, D. L. Danilov and P. H. L. Notten, *Adv. Energy Mater.* **2020**, *10*, 1–11.
[21] C. Vaalma, D. Buchholz, M. Weil and S. Passerini, *Nat. Rev. Mater.* DOI:10.1038/natrevmats.2018.13.
[22] F. Duffner, L. Mauler, M. Wentker, J. Leker and M. Winter, *Int. J. Prod. Econ.* **2021**, *232*, 107982.
[23] L. Xie, C. Tang, Z. Bi, M. Song, Y. Fan, C. Yan, X. Li, F. Su, Q. Zhang and C. Chen, *Adv. Energy Mater.* **2021**, *11*, 1–22.
[24] U. S. Geological Survey, *Mineral commodities summary 2024: U. S. Geological Survey* **2024**.
[25] C. Xu, Y. Ma, J. Zhao, P. Zhang, Z. Chen, C. Yang, H. Liu and Y. S. Hu, *Angew. Chem. Int. Ed.* DOI:10.1002/anie.202217761.
[26] M. Li, M. Gaboardi, A. Mullaliu, M. Maisuradze, X. Xue, G. Aquilanti, J. R. Plaisier, S. Passerini and M. Giorgetti, *ChemSusChem* DOI:10.1002/cssc.202300201.
[27] Y. Shang, X. Li, J. Song, S. Huang, Z. Yang, Z. J. Xu and H. Y. Yang, *Chem* **2020**, *6*, 1804–1818.
[28] L. Samain, F. Grandjean, G. J. Long, P. Martinetto, P. Bordet and D. Strivay, *J. Phys. Chem. C* **2013**, *117*, 9693–9712.
[29] F. M. Maddar, D. Walker, T. W. Chamberlain, J. Compton, A. S. Menon, M. Copley and I. Hasa, *J. Mater. Chem. A* **2023**, 15778–15791.
[30] I. Nielsen, D. Dzodan, D. O. Ojwang, P. F. Henry, A. Ulander, G. Ek, L. Häggström, T. Ericsson, H. L. B. Boström and W. R. Brant, *J. Phys. Energy* **2022**, *4*, 044012.
[31] D. O. Ojwang, M. Svensson, C. Njel, R. Mogensen, A. S. Menon, T. Ericsson, L. Häggström, J. Maibach and W. R. Brant, *ACS Appl. Mater. Interfaces* **2021**, *13*, 10054–10063.
[32] L. Hartmann, J. Deshmukh and M. Metzger, *J. Electrochem. Soc.* **2023**, *170*, 030540.
[33] F. M. Maddar, D. Walker, T. W. Chamberlain, J. Compton, A. S. Menon, M. Copley and I. Hasa, *J. Mater. Chem. A* DOI:10.1039/d3ta02570e.
[34] S. L. Dreyer, F. M. Maddar, A. Kondrakov and J. Janek, DOI:10.1002/batt.202300595.
[35] S. Baumgart, M. Sotoudeh and A. Groß, *Batteries & Supercaps* DOI:10.1002/batt.202300294.
[36] X. Guo, Z. Wang, Z. Deng, X. Li, B. Wang, X. Chen and S. P. Ong, *Chem. Mater.* **2019**, *31*, 5933–5942.
[37] F. Wang, Z. Lin, L. Liu, X. Wei, S. Lin, L. Dai, Y. Wei, C. Liang and B. Liaw, *J. Electrochem. Soc.* **2020**, *167*, 090549.
[38] S. Buechele, E. Logan, T. Boulanger, S. Azam, A. Eldesoky, W. Song, M. B. Johnson and M. Metzger, *J. Electrochem. Soc.* **2023**, *170*, 010518.
[39] F. Feng, S. Chen, S. Zhao, W. Zhang, Y. Miao, H. Che, X. Z. Liao and Z. F. Ma, *Chem. Eng. J.* **2021**, *411*, 128518.
[40] B. Rowden and N. Garcia-Araez, *Energy Reports* **2021**, *7*, 97–103.
[41] E. Lyle, R. Vaeli, M. Cormier and M. Metzger, *J. Electrochem. Soc.* **2022**, *169*, 060527.
[42] J. Klemens, A. K. Wurba, D. Burger, M. Müller, W. Bauer, S. Büchele, O. Leonet, J. A. Blázquez, I. Boyano, E. Ayerbe, H. Ehrenberg, J. Fleischer, A. Smith, P. Scharfer and W. Schabel, *Batteries & Supercaps* DOI:10.1002/batt.202300291.
[43] P. Stüble, C. Müller, N. Bohn, M. Müller, A. Hofmann, T. Akçay, J. Klemens, A. Koeppe, S. Kolli, D. Rajagopal, H. Geßwein, W. Schabel, P. Scharfer, M. Selzer, J. R. Binder and A. Smith, *Batteries & Supercaps* DOI:10.1002/batt.202400406.
[44] C. Müller, Z. Wang, A. Hofmann, P. Stüble, X. Liu-Théato, J. Klemens and A. Smith, *Batteries & Supercaps* DOI:10.1002/batt.202300322.
[45] H. Geßwein, P. Stüble, D. Weber, J. R. Binder and R. Mönig, *J. Appl. Crystallogr.* **2022**, *55*, 503–514.

Manuscript received: January 30, 2025
Accepted manuscript online: February 25, 2025
Version of record online: March 18, 2025